2.1. CONDENSED MATTER PHYSICS

CONTENTS

2.2. Neutron Nuclear Physics

CONTENTS

NEUTRON DIFFRACTION STUDY OF STRUCTURAL CHANGES IN AMMONIUM HALIDES ND_4Br AND ND_4Cl UNDER HIGH PRESSURE

A.M.BALAGUROV, D.P.KOZLENKO, B.N.SAVENKO
FLNP, JINR, 141980, Dubna, Russia.

V.P.GLAZKOV, V.A.SOMENKOV
RRC "Kurchatov Institute", 123182, Moscow, Russia

The ammonium halides NH_4Br, NH_4Cl, NH_4I and their deuterated analogs have attracted a great deal of attention in the scientific literature. They show a number of phases[1] and the order-disorder phase transition (λ-transition) was proved to be of great interest[2].

Structural changes in ammonium halides ND_4Br at pressures up to 45 кbar and ND_4Cl up to 35 kbar have been studied with the DN-12 diffractometer[3]. The samples were placed between sapphire anvils[4], which were used to create the pressure. The sample volumes were 2.5 mm^3. Two ring-shaped detectors (16 independent ^3He-counters in each ring) 800 and 700 mm in diameter were used to gather the scattered neutrons. The scattering angles were 45° and 90°; the diameter of the incident beam was 2 mm. All the experiments were performed at room temperature. The pressure was measured by a ruby fluorescence technique.

A orientational phase transition from the phase in which the ammonium tetrahedra are randomly oriented (CsCl-type cubic structure, space group Pm3m) into the phase in which the ammonium tetrahedra are oriented in parallel (CsCl-type cubic structure, space group P-43m), for ND_4Br at the pressure 26<P<31 kbar and ND_4Cl at the pressure P<13 kbar was observed, in agreement with the previous investigations by other methods.

The obtained equations of state with the ones for nondeuterated systems NH_4Br and NH_4Cl obtained by piston-displacement technique[5] are shown in fig.1.

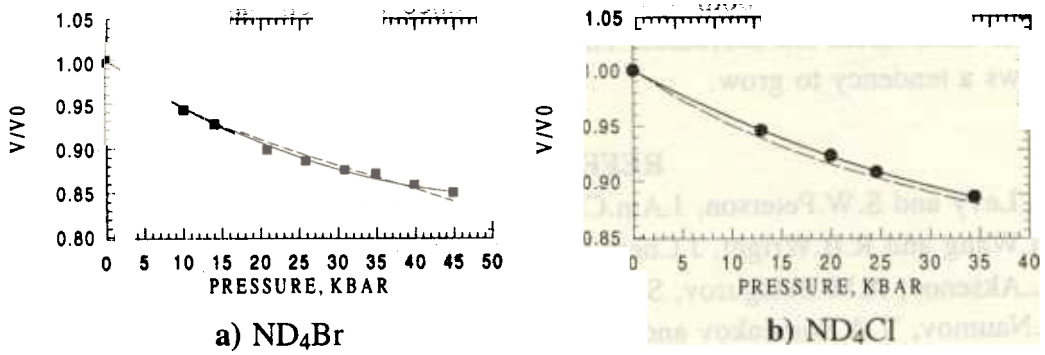

***Fig.1** Equations of state for ND_4Br (■) and ND_4Cl (●) with the data for NH_4Br and NH_4Cl (------) taken from ref.[5].*

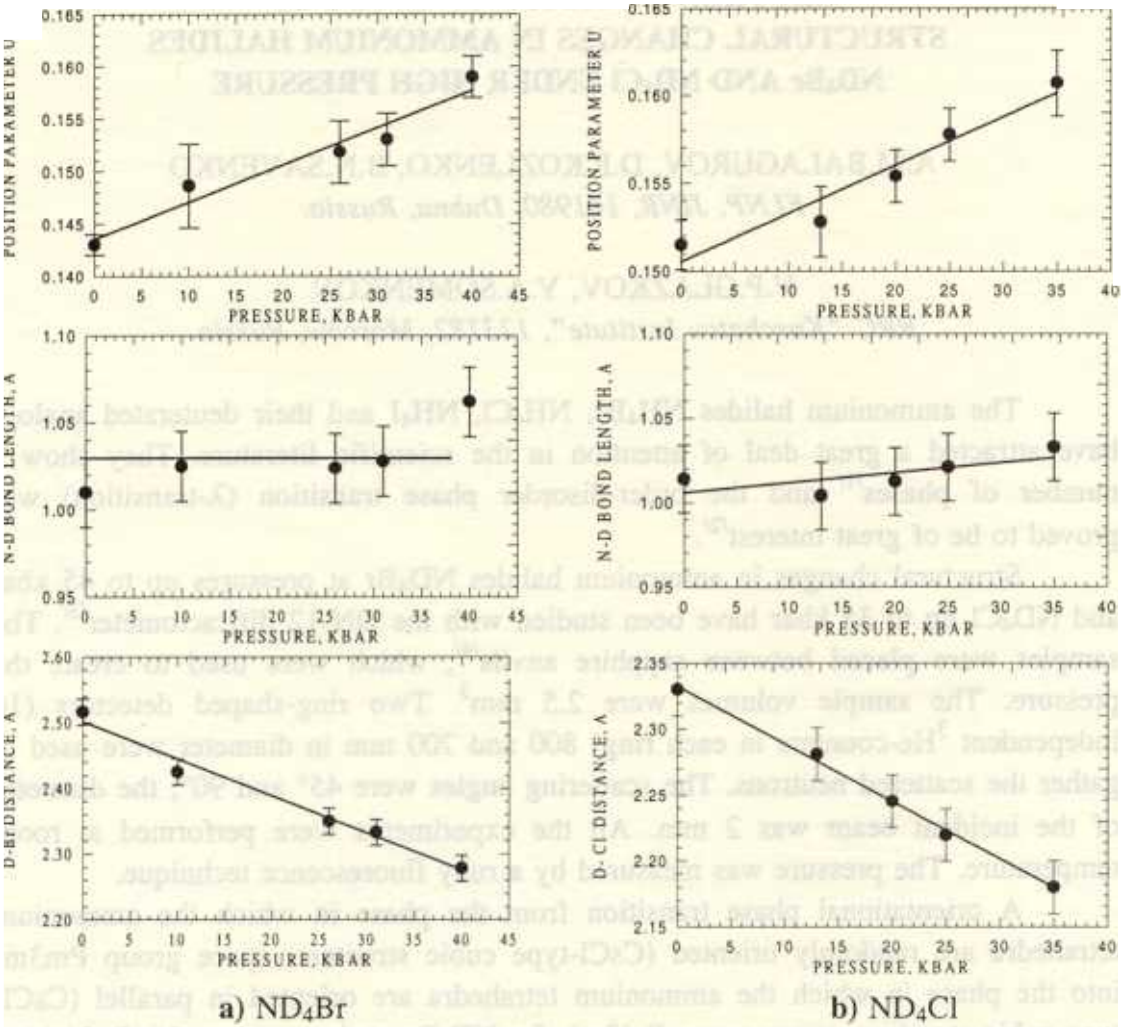

Fig.2 Position parameter, N-D bond length and D-Br (D-Cl) interatomic distance as functions of pressure.

Position parameter, N-D bond length and D-Br (D-Cl) interatomic distance as functions of pressure are shown in fig.2.

Under pressure, in both systems the distance between halide ions and the molecular ammonium ion decreases. The N-D bond length remains nearly the same but shows a tendency to grow.

REFERENCES

1 H.A.Levy and S.W.Peterson, J.Am.Chem.Soc. 75, 1536 (1953)

2 C.H.Wang and R.B.Wright, J.Chem.Phys. 57, 4401 (1972)

3 V.L.Aksenov, A.M.Balagurov, S.L.Platonov, B.N.Savenko, V.P.Glazkov, I.V.Naumov, V.A.Somenkov and G.F.Syrykh, High Pressure Research 14, 181 (1995)

4 V.P. Glazkov and I.N.Goncharenko, Fizika i tehnika vysokih davlenij (in russian), 1, 56, (1991)

5 S.N.Vaidya and G.C.Kennedy, J.Phys.Chem.Solids, 32, 951, (1971)

RESIDUAL STRESS STUDIES AT THE NEUTRON HIGH RESOLUTION FOURIER DIFFRACTOMETER

V.L.Aksenov[1], A.M.Balagurov[1], G.D.Bokuchava[2], M.Kröning[3], J.Schreiber[3], N.R.Shamsutdinov[1], Yu.V.Taran[1]

[1] Frank Laboratory of Neutron Physics, JINR, 141980 Dubna, Russia
[2] Institute for Nuclear Research of RAS, 117312 Moscow, Russia
[3] Fraunhofer Institute for Nondestructive Testing, W-6600 Saarbrücken, Germany

Introduction

Putting into operation in 1992 of high resolution Fourier diffractometer (HRFD) [1] at the IBR-2 pulsed reactor has allowed to begin realization of the residual stress investigation program in bulk samples for industrial applications [2]. HRFD includes the following equipment: four detectors at the scattering angles of ±90°(the solid angles of 28 and 7 msr) and ±152° (the solid angle of 80 msr each), 4-axis (x,y,z,ω) neutron scanner for simple experiments, two multi-slit radial collimators with gauge volume resolution of 2 mm for both ±90°-detectors, load testing machine and nitride boron slit systems. In nearest future 5-axis (x,y,z,ω,Ω) "HUBER" goniometer will be used for full strain tensor measurements. High neutron flux at the sample position (~10^7 n/cm^2/s) and high d-spacing resolution ($\Delta d/d=1\cdot10^{-3}$ at $2\theta=\pm152°$ and $4\cdot10^{-3}$ at $2\theta=\pm90°$ for d=2 Å) of HRFD gives a possibility for precise strain measurements within reasonable beam time. A combination of the time-of-flight technique and two-detector system at the scattering angles ±90° allows one to measure a large number of reflections simultaneously in two mutually perpendicular directions. With the help of these detectors measurements of residual stresses were performed in some samples for the industrial application.

Research program is realized in the frame of the agreement between FLNP, Dubna and FINT, Saarbrücken. This report describes some experiments for residual stress investigation performed at HRFD during last 2 years.

Austenitic steel tube with a welded ferritic cover

Shape welding is an interesting alternative method for manufacturing, but the existence of uncontrollable residual stress distributions in welded materials prevents its wide application. On the other hand, shape welded ferritic layers on austenitic tubes can help suppress stress corrosion because these layers produce compressive stress states on the austenitic tube. The analysis of residual stresses through the ferritic weld into the austenitic material can be helpful for the optimization of the corresponding welding technique.

Seven layers of the ferritic steel with 135 welding traces and a total cover length of 1100 mm were welded on a 15 mm thick austenitic steel tube with an outer radius of 148 mm. The outer radius of the whole manufactured two-layer tube was 168 mm. The sample with the size of 10×30×35 mm^3 was cut from this tube (fig. 1).

Two orthogonal strain components can be measured simultaneously by two detectors at the scattering angles of ±90°. Since the aim of the study was to compare the data obtained by neutron diffraction method with those by the destructive turning out method and the theoretical predictions by the finite element method, it had sufficed to measure strains only in two orthogonal directions of the scattering vector **Q**. In our case, these were the radial (ε_{rad}) and tangential (ε_{tan}) strain components. Strain scanning in a radial direction (x-axis) across the weld to a depth of 2 mm from the surface of the sample was conducted with the neutron scanner. To form the direct beam, a boron nitride diaphragm with a slit of 2 mm wide by 20 mm high was installed at the exit of a mirror neutron-guide. To set the scattered beams at ±90°, diaphragms with a slit width of 2 mm were

installed at a distance of 42 mm from the center of the diffractometer. The gauge volumes formed by these diaphragms were 2.1×4.5×19.4 and 2.1×2.6×19.4 mm^3 for the +90° and the -90° detectors, respectively.

From experimental data it is easy to calculate the difference between the tangential and radial components of the stress tensor $\sigma_{tan}-\sigma_{rad}=E(1+\nu)^{-1}(\varepsilon_{tan}-\varepsilon_{rad})$ (under the elastic model assumption). For the ferritic part (α-phase), good agreement of the neutron data with the results of other methods was found (fig.2). For the austenitic part (γ-phase), disagreement is obviously due to uncontrollable influence of II.kind microstresses on the neutron results.

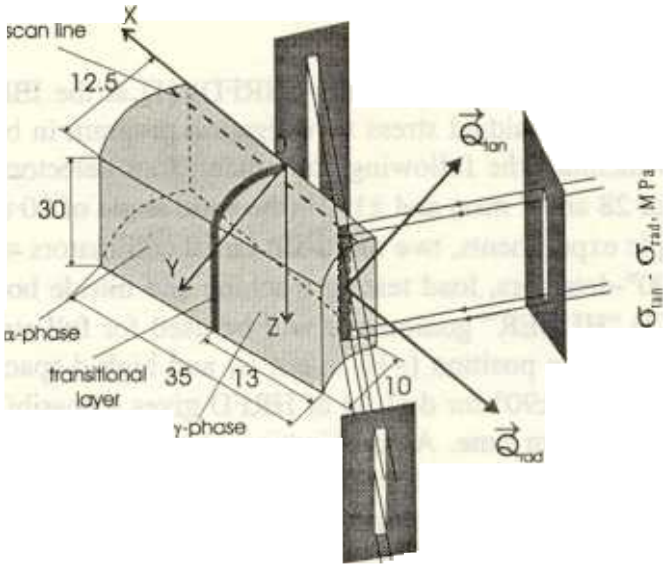

Fig. 1. The investigated sample and the (x,y,z) sample-related coordinate system.

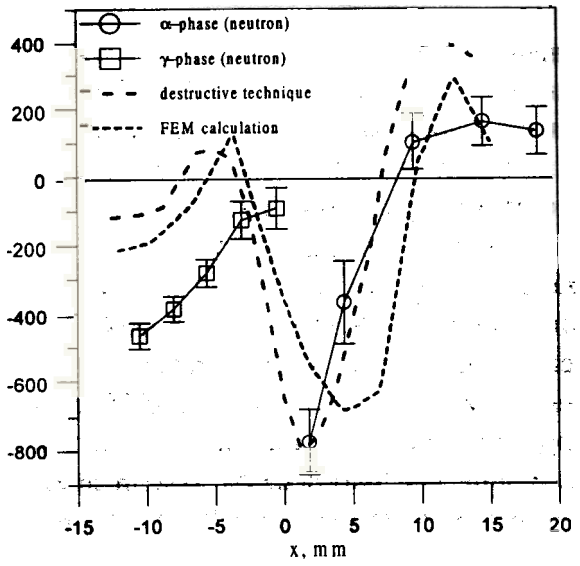

Fig. 2. The dependence of $\sigma_{tan}-\sigma_{rad}$ on the coordinate x, where x=0 corresponds to the transition layer.

In summary it should be noted that the first neutron diffraction investigations of residual stresses in shape welded tubes yielded satisfactory results. Qualitative and even quantitative agreement with the destructive turning out method results, as well as the FEM calculations can be acknowledged. However, in subsequent investigations a more complete analysis of the residual stress state can be expected. It is planned to measure all three stress components with a larger tube segment. For this purpose, the so called $\sin^2\psi$-method will be applied using X-ray and neutron diffraction techniques. In addition, it would be useful to determine the elastic constants for the both phases by carrying out a tensile test experiment.

Neutron elastic constants

Austenitic stainless steels are widely used because of their high corrosion resistance and toughness. High resolution neutron diffraction was applied to estimate the mechanical properties of austenitic stainless steel and to determine neutron elastic constants of the given material. The examined material was an austenitic stainless steel X6CrNiTi1810 of the following content (wt %): C - 0.04, Si - 0.44, Mn - 1.14, P - 0.033, S - 0.004, Cr - 17.74, Ni - 19.3, Ti - 0.35. The investigated sample of austenitic steel was subjected to a load in situ in the neutron beam, using a special purpose testing machine. The elastic strain was measured for different crystal planes (hkl), parallel and perpendicular to the applied load direction (fig. 3). From the slopes of the strain-stress linear dependencies the elastic modules $E_{||}$ and $E_{\perp}$ as a function of the anisotropy factor $\Gamma_{hkl}=(h^2k^2+h^2l^2+k^2l^2)/(h^2+k^2+l^2)^2$ were obtained (fig. 4). The strains determined from the lattice parameter changes by the Rietveld profile refinement technique and corresponding to the anisotropy

factor Γ_{hkl}=0.2 are also included. The elastic constants S_{11}, S_{12} and S_{44} were calculated in the frame of the Hill model which assumes taking of an arithmetic average of the Reuss and Voigt model values and gives the results very close to the Kröner model values. Thus, the following values were obtained: $S_{11}=6.70\times10^{-6}$ MPa^{-1}, $S_{12}=-2.24\times10^{-6}$ MPa^{-1}, and $S_{44}=12.43\times10^{-6}$ MPa^{-1}.

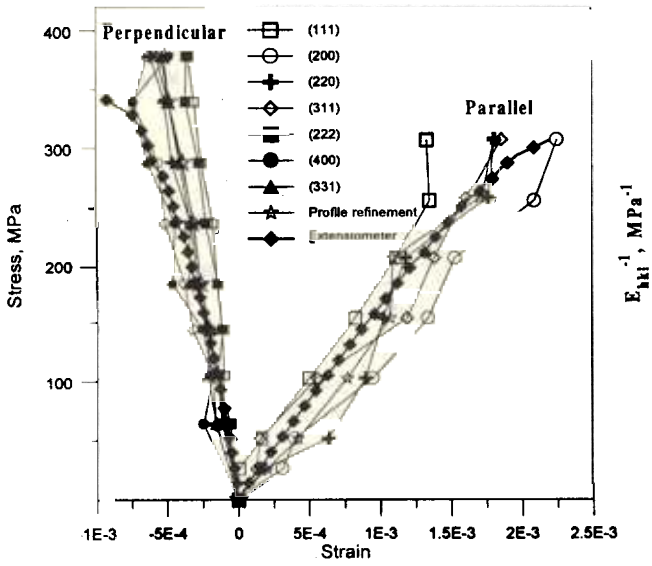

Fig. 3. Stress-strain relationships for different reflections (hkl) measured in direction parallel and perpendicular to the applied load.

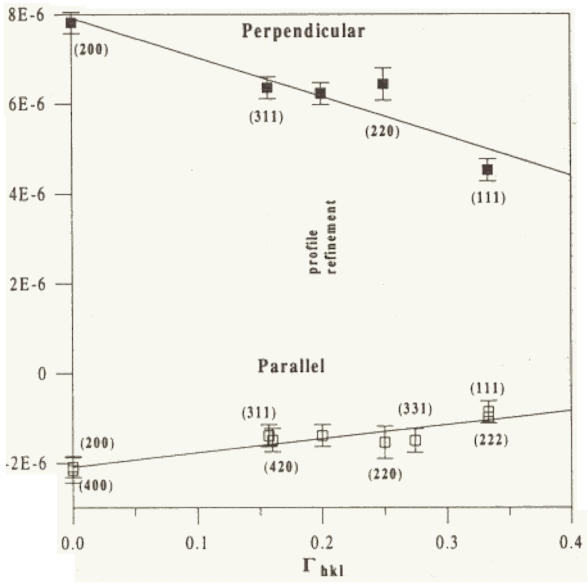

Fig. 4. Dependence of the elastic modules $E_{||}$ and $E_{\perp}$ parallel and perpendicular to the applied load versus the anisotropy factor Γ_{hkl}.

Austenitic steel samples with different degree of low cycle fatigue

The influence of applied cyclic load on the materials mechanical properties is of great current interest. In order to investigate residual stress evolution a series of the austenitic steel samples with different degree of low cycle fatigue was studied. The cylindrical samples produced from austenitic stainless steel X6CrNiTi1810 (see above) were subjected to a number of tensile-compressive loading cycles with a maximum plastic deformation of ± 0.6% at the frequency of 0.1 Hz. The number of cycles corresponding to the sample failure was $N_{max}\approx1020$. As is well known, as a result of thermal treatment or plastic deformation, austenitic stainless steel undergoes a phase transition to the tetragonal martensitic phase. The tetragonal distortion value for the martensitic structure strongly depends on the carbon content. In our experiment due to a low carbon content only the diffraction peaks characteristic for a martensitic cubic structure were registered. An increase in the martensite volume fraction was observed at an increase in the cycle fatigue degree N/N_{max} (fig. 5). The data were obtained from the Rietveld profile refinement. The residual strain for both phases was measured in the longitudinal and radial directions. It was assumed that the stress field distribution in the sample had the cylindrical symmetry. The stresses calculated from the (311) and (220) reflections for austenite and martensite, respectively, are shown in fig. 6. For an austenitic matrix, the elastic constants determined from the previous experiment were used and for martensite were taken from the literature. It is necessary to note that stresses in austenite are mainly compressive while stresses in the martensite phase are tensile.

The analysis of the diffraction peak broadening point to a partial relaxation of estimated microstresses as the fatigue degree increases. Most likely this phenomenon is connected with a growth of microcracks in the bulk of the material. For a more brittle martensitic phase, this effect is more pronounced in comparison with austenite. Usually after plastic deformation the martensite phase produces a structure of oriented plates or laths. Therefore martensite texture formation during

phase transition can be expected. Indeed the registered neutron diffraction spectra from austenitic fatigued samples shown texture presence and its variation in dependence of the fatigue degree. Consequently further detailed researches will be devoted to the quantitative analysis of the texture evolution in dependence of fatigue degree and its influence on the residual stress distribution.

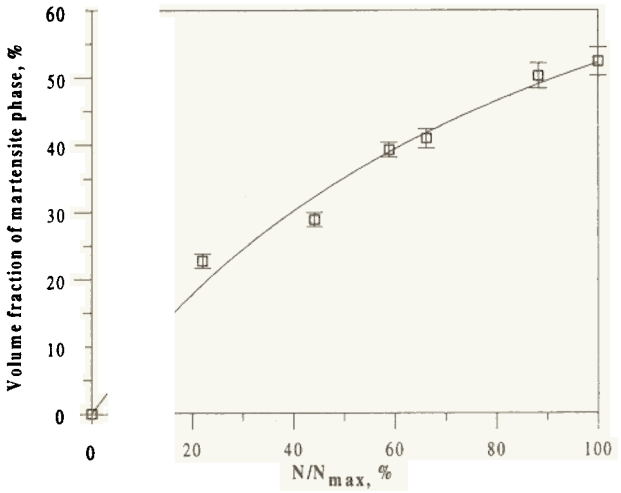

Fig. 5. Dependence of the martensitic volume fraction versus the fatigue degree. The line serves as a guide for the eye.

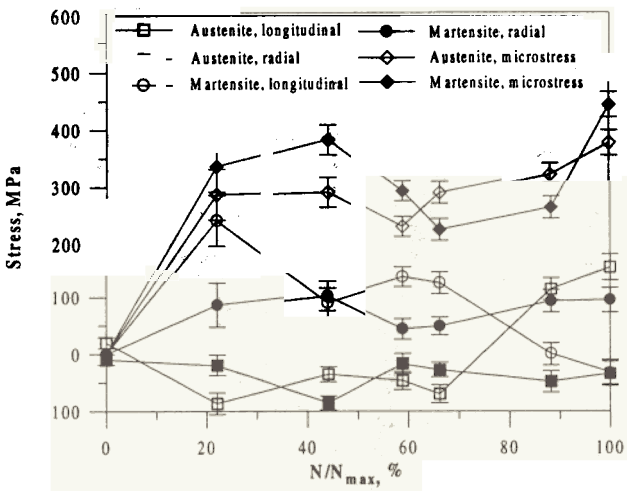

Fig. 6. Phase stresses and microstresses versus the fatigue degree

Other experiments

The functionally gradient materials (FGM) as well as composites are very promising type of advanced materials with enhanced properties. It is obvious that the mixture of materials with rather different parameters of thermal expansion is followed by the appearance of residual stresses, which have to be controlled. At the HRFD the structural changes and the variation of the residual stresses in different W-Cu and SiC-$MoSi_2$ gradient samples, prepared by an anode oxidation of porous electrodes and other methods, were studied. The samples were scanned by neutron beam with spatial resolution of ~1 mm in gradient direction. The tungsten and silicon carbide volume content and macrostress component changes were estimated from Rietveld profile refinement.

Another interesting type of material studied at HRFD are composites with Al infiltration in porous Al_2O_3 matrix (the matrix porosity degree was 15%, 25% and 35). The analysis of Al diffraction peak intensities revealed sharp texture presence for this phase while in the matrix phase the preferred orientation was absent. The total profile refinement results which corresponds to averaging on all (hkl) directions are compared with ones obtained from separate diffraction peak processing, which enables to estimate the intergranular stress fluctuations.

To obtain information on the stress state at the interface of a Si-chip on a Al_2O_3 substrate the neutron and X-ray diffraction results were combined. The residual stresses in Al_2O_3 plate are due to the housing of the Si-chip by an epoxidic layer. The results fit quite well with the FEM simulation.

References

[1] V.L.Aksenov, A.M.Balagurov, V.G.Simkin, Yu.V.Taran, V.A.Trounov, V.A.Kudrjashev, A.P.Bulkin, V.G.Muratov, P.Hiismaki, A.Tiitta, O.Antson. The new Fourier diffractometer at the IBR-2 reactor: design and first results. Proc. of ICANS-XII (Abingdon), 1993, vol.1, p.124.

[2] V.L.Aksenov, A.M.Balagurov, V.G.Simkin, Yu.V.Taran, V.A.Trounov, V.A.Kudrjashev, A.P.Bulkin, J.Schreiber. On determination of residual stresses with the high resolution Fourier diffractometer at the IBR-2 reactor. Applied Crystallography, Proc. of XVI Confer. (Cieszyn), World Scientific, 1995, p.120.

INVESTIGATION OF $Y_{0.7}PR_{0.3}BA_2CU_3O_{6+X}$ STRUCTURE UNDER PRESSURES UP TO >3 GPA

V.N.Narozhnyj[a], A.M.Balagurov[b], B.N.Savenko[b], D.V.Sheptyakov[b], V.P.Glazkov[c]

[a]*Institute for High Pressure Physics, Troitsk*
[b]*FLNP, Joint Institute for Nuclear Research, Dubna*
[c]*Russian Scientific Center "Kurchatov Institute", Moscow*

We have studied the powder sample of $Y_{0.7}Pr_{0.3}Ba_2Cu_3O_{6+x}$ (further, Y(Pr)-123), prepared in the Institute for high pressure physics (Troitsk). The content of an extra oxygen in it was close to 0.9. Later this value as well as the stoichiometry of the compound were proved to be realistic from the point of view of neutron diffraction at ambient pressure in different scattering regimes (forward, perpendicular and back scattering) and were fixed to the exact values at all the refinements at high pressure.

We used the sapphire-anvils high pressure cell (designed at the RRC "Kurchatov Institute") to create the desirable pressures at the sample. The pressure was measured by detecting the displacement of the ruby luminescence lines; the uncertainty of these determinations was 0.05 GPa (0.5 kbar).

The experiments with the sample were carried out at the DN-12 [1] time-of-flight diffractometer specialized for microsample investigations at the IBR-2 pulsed reactor in Dubna. For each pressure, the neutron diffraction patterns were collected at two different angles simultaneously (usually near 45° and 90°). Besides that the whole series of measurements at ambient pressure were made at different scattering angles from 45° to 138° (covering the range of d_{hkl} from 1.0 to 5.0 E) on a sample with a volume of approximately 20 mm^3 in order to purify the peculiarities of the original structure (stoichiometry of the compound, thermal parameters of different atoms). As all the refinements at ambient pressure gave practically identical results these values were fixed to the ideal values at all the refinements at high pressure. The experiments in the high pressure cell (sample volume $\leq$2 mm^3) were carried out at pressures of 1.5, 2.8 and 3.3 GPa in the regions of d_{hkl} from 1.8 to 5.0 E (at scattering angle 2Θ=45°) and from 0.95 to 2.56 E (at scattering angle 90°). The later regions of the diffraction patterns were processed with the Rietveld method as containing the greater number of the Bragg reflections.

Rietveld refinement treatments of the diffraction patterns obtained at zero pressure at the DN-12 diffractometer were used to estimate the values of the initial lattice parameters and the atoms coordinates in the structure. The treatment of data obtained at high pressures gave us the information about the structural changes caused by applying the high external pressure to the system. A view of parts of the Rietveld refinements for the Y(Pr)-123 structure at zero pressure and at pressure 3.3 GPa are shown in fig. 3. Detailed results of the diffraction pattern treatments at pressures 0, 1.5, 2.8 and 3.3 GPa are presented in the table 1.

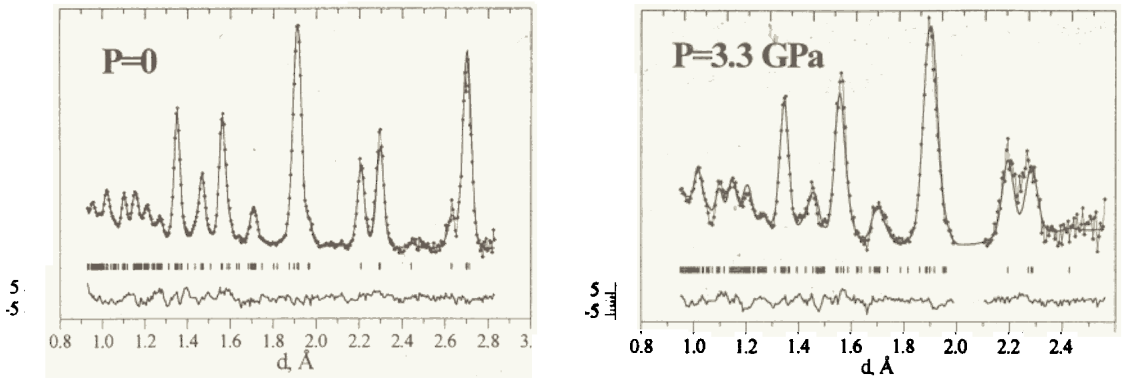

Fig. 1. The diffraction patterns of the Y(Pr)-123 measured at different pressures at the DN-12 diffractometer and processed with Rietveld method. The scattering angle 2θ≈90°. Experimental points, calculated and weighted difference profiles are shown. The ticks at the bottom of the graphs correspond to the positions of the calculated Bragg peaks.

Table

Refined structural parameters of Y(Pr)-123 ceramics at different pressures.
Instrument: DN-12. 2Θ=90 deg.

Parameter \ Press.	**0 kbar**	**15 kbar**	**28 kbar**	**33 kbar**
2Θ, deg	45°, 90°, 138°	90°	90°	90°
a, E	3.824(3)	3.787(3)	3.768(4)	3.769(3)
b, E	3.863(4)	3.844(5)	3.827(5)	3.827(3)
c, E	11.563(12)	11.462(18)	11.38(18)	11.380(15)
V, E^3	170.810	166.855	164.101	164.626
d_{hkl} – range, E	0.93 – 4.35	0.95 – 2.56	0.95 – 2.56	0.95 – 2.56
Y(0.5,0.5,0.5), n	0.7	0.7	0.7	0.7
Pr(0.5,0.5,0.5), n	0.3	0.3	0.3	0.3
Ba(0.5,0.5,z), z	0.181(2)	0.176(3)	0.168(3)	0.165(2)
Cu1(0,0,0), n	1	1	1	1
Cu2(0,0,z), n	2	2	2	2
z	0.359(2)	0.355(2)	0.358(2)	0.356(1)
O1(0,0,z), z	0.163(2)	0.158(3)	0.155(3)	0.155(2)
O2(0.5,0,z), z	0.374(5)	0.376(5)	0.379(4)	0.378(4)
O3(0,0.5,z), z	0.378 (4)	0.369(7)	0.369(7)	0.377(4)
O4(0,0.5,0), n	0.9	0.9	0.9	0.9

The obtained dependencies of the lattice constants on pressure are presented in the figs. 4 and 5. As it can be seen from the table 1, the only changes in the structure visible within the experimental and statistical errors are the displacements of the Ba atoms and of the oxygen O1 atoms in barium-containing planes. The dependencies of this coordinates on pressure are presented in the fig. 6. It is obvious that the compressing of the structure corresponds to the prior compressing of the crimped BaO plane. The absolute value of this splitting reduces by almost 45% under the pressure of 3.3 GPa.

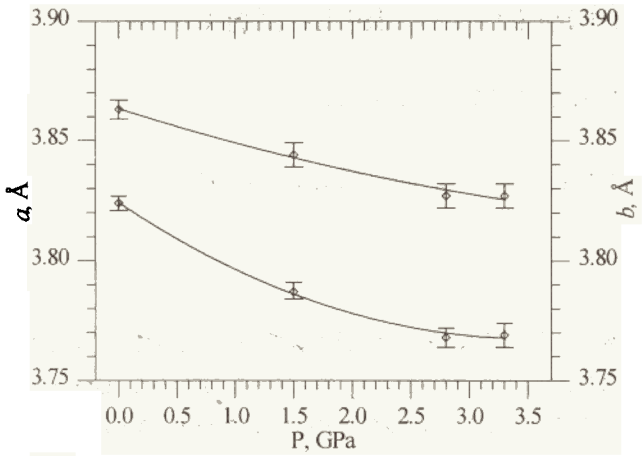

*Fig. 2. Dependencies of lattice constants **a** and **b** of Y(Pr)-123 structure versus pressure.*

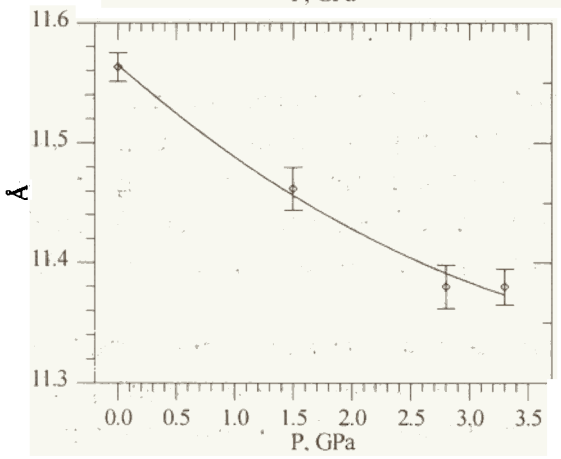

*Fig. 3. Dependence of lattice constant **c** of Y(Pr)-123 structure versus pressure.*

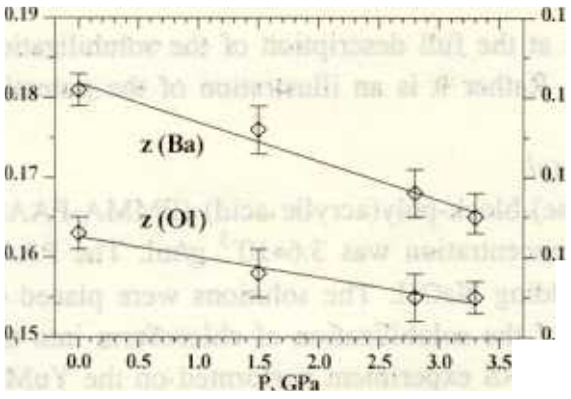

Fig. 4. Dependencies of the z-coordinates of Ba and O1 atoms in Y(Pr)-123 structure versus pressure.

V.L.Aksenov, A.M.Balagurov, S.L.Platonov, B.N.Savenko, V.P.Glazkov, I.V.Naumov, V.A.Somenkov, G.F.Syrykh, High Press. Res. 14 (1995) 181

Time-resolved SANS study of kinetics of solubilization

J. Plestil, H. Pospisil, M. Steinhart, M.A. Kiselev*

Institute of Macromolecular Chemistry, Academy of Sciences of the Czech Republic, Heyrovsky Sq.2, 162 06 Prague
**FLNP, JINR, 141980 Dubna Russia*

It has been known for some time that amphiphilic block copolymers consisting of one hydrophilic and one hydrophobic block form micelles with relatively narrow size in aqueous media. The ability of these micelles to solubilize various hydrophobic organic molecules, which has been studied by several techniques, is one of their important and interesting properties.

SANS has proven to be an extremely useful method for the structural studies on the micellar systems, including various aspects of the solubilization phenomenon. This technique provides not only the parameters characterizing micelle as a whole (mass, radius of gyration) but also an information about its internal structure (radius of micelle core and shell). These parameters are varying during solubilization can therefore be used for the description of this process.

Full understanding of the solubilization phenomenon is not possible without studying of its kinetics. The SANS technique can be employed to this purpose, if the scattering data can be taken rapidly enough. The YuMO TOF SANS spectrometer at the JINR, Dubna is an excellent instrument for such studies.

This short experimental report is not aimed at the full description of the solubilization of hydrophobic compound in the micellar solution. Rather it is an illustration of the potential of the YuMO spectrometer.

Experimental

Micelles formed by poly(methyl methacrylate)-block-poly(acrylic acid) (PMMA-PAAc) copolymer in D_2O were studied. The copolymer concentration was $3.6 \bullet 10^{-3}$ g/ml. The PAAc component was neutralized to various degree by adding NaOH. The solutions were placed in the optical cells with a path length 2mm. Kinetics of the solubilization of chloroform into the micellar solutions was followed in a time-resolved SANS experiment performed on the YuMO spectrometer.

Results

The copolymer forms micelles with PMMA core and PAAc corona in aqueous media. Solubilization into these micelles was studied for six samples with various degrees of neutralization simultaneously. The exposure time was 2 minutes per one spectrum. The resulting scattering curves provided the radii of the micellar cores for the intitial solutions and their variation with progressing solubilization of chloroform. The results for three degrees of neutralization are shown in Figure 1. In the absence of solubilizate the core radius decreases with increasing degree of neutralization α. However, preliminary NMR measurements suggest that PMMA cores are in frozen state. Thus it is likely, that the actual size of the cores is

independent of α. This discrepancy can be explained by a partial adhesion of the inner part of the corona chains (PAAc) to the PMMA core. To check this hypothesis we plan to perform similar measurements on the copolymer samples with one labelled block. Progressing solubilization of chloroform is reflected by increasing radius of the micelle core. For example, for α=0 the radius starts from the initial value of 78 Å and reaches the saturated value of 93 Å within two hours.

The described experiment shows that the YuMO spectrometer is a powerful instrument not only for the static studies but also for the time resolved experiments with the temporal resolution in the order of a minute. This is true even for not too strong scatterers like for example the dilute solutions investigated here.

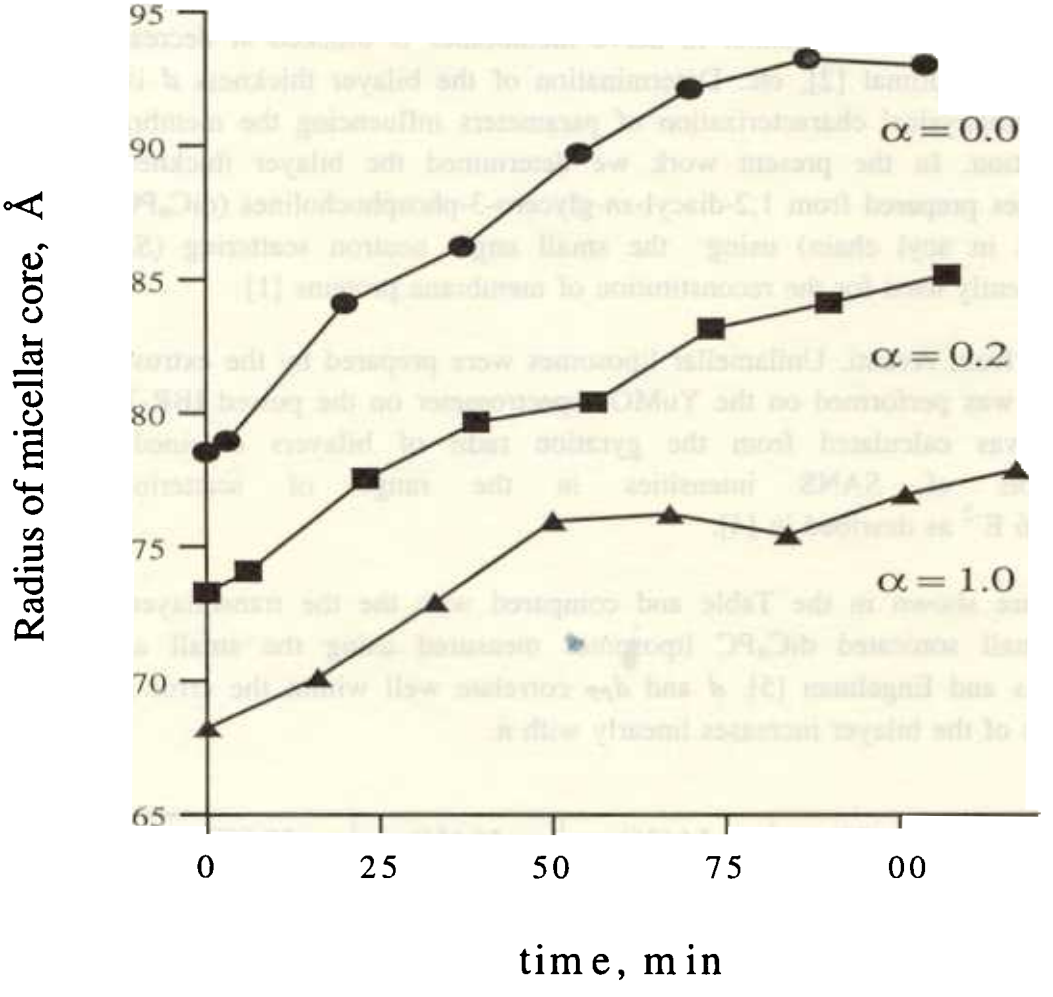

Fig.1 Variation the micellar radius during solubilization of chloroform into PMMA/PAAc micelles at chosen degrees of neutralization α. The mean radius was determined by the fitting of the experimental SANS data to the theoretical scattering curve of homogeneous spheres with a Schulz-Zimm distribution of radii.

BILAYER THICKNESS IN EXTRUDED UNILAMELLAR DIACYL-PHOSPHATIDYLCHOLINE LIPOSOMES: SANS STUDY

DUBNIKOV B.M., KISELEV M.[1], BALGAV P.

Faculty of Pharmacy, Comenius University, 83232 Bratislava (Slovakia)

[1]*Frank Laboratory of Neutron Physics, Joint Institute of Nuclear Reseach, Dubna (Russia*

Thickness of the lipid bilayer in biological membranes profoundly affects properties of transmembrane proteins. For example, the (Ca-Mg)ATPase from muscle sarcoplasmic reticulum displays maximum activity at particular bilayer thickness; the activity decreases in thinner or thicker bilayers [1], the sodium channel in nerve membranes is blocked at decreased bilayer thickness smaller than optimal [2], etc. Determination of the bilayer thickness ***d*** is thus very important for the biophysical characterization of parameters influencing the membrane protein structure and function. In the present work we determined the bilayer thickness in large unilamellar liposomes prepared from 1,2-diacyl-*sn*-glycero-3-phosphocholines (diC_nPC, ***n*** is the number of carbons in acyl chain) using the small angle neutron scattering (SANS). The liposomes are frequently used for the reconstitution of membrane proteins [1].

Lipids were from Avanti. Unilamellar liposomes were prepared by the extrusion method in D_2O [3]. SANS was performed on the YuMO spectrometer on the pulsed IBR-2 reactor in JINR Dubna. ***d*** was calculated from the gyration radii of bilayers obtained from the Kratky-Porod plots of SANS intensities in the range of scattering vectors $0.001\ E^{-2} \leq Q^2 \leq 0.006\ E^{-2}$ as desribed in [4].

The values of ***d*** are shown in the Table and compared with the the transbilayer phosphate spacing d_{PP} in small sonicated diC_nPC liposomes measured using the small angle X-ray scattering by Lewis and Engelman [5]. ***d*** and d_{PP} correlate well within the error of methods used. The thickness of the bilayer increases linearly with ***n***.

n (°C)	***12*** (20)	***14*** (36)	***16*** (44)	***18*** (60)
d	32.4±0.2 Å	34.2±0.2 Å	37.3±0.2 Å	39.8±0.2 Å
d_{PP}	30.5±1.0 Å	34.0±1.0 Å	37.0±1.0 Å	40.5±1.0 Å

1. Lee A.G., East J.M., Balgav P., Pest. Sci. 32, 317-327, 1991
2. Hendry B.M., Elliott J.R., Haydon D.A., Biophys. J., 47, 841-845, 1985
3. Gordeliy V.I., Golubchikova L.V., Kuklin A., Syrykh A.G., Watts A. Progr. Colloid Polym. Sci. 93, 252-257, 1993
4. MacDonald R.C., MacDonald R.I., Menco B.Ph.M., Takeshita K., Subbarao N.K., Hu L.-R., Biochim. Biophys. Acta 1061, 297-303, 1991
5. Lewis B.A., Engelman D.M., J. Mol. Biol. 166, 211-217, 1983

Critical Fluctuations of Lipid Membranes

V.I.Gordeliy, V.G.Cherezov
FLNP, JINR, 141980, Dubnà, Russia

Fluctuations are vital in biological macromolecules such as proteins, DNA and RNA. Fluctuations of biological membranes also seems to be important for some processes in living cell. When immersed in water lipid membranes form closed bilayer vesicles, performing small thermal undulations, governed by bending modulus of the membrane. These fluctuations can be highly enlarged by increasing the temperature or by approaching to the temperature of main phase transition. Melting of hydrocarbon chains in lipid membranes is first kind phase transition, which temperature is closed to the critical point. Near to this point in-plane density fluctuations are enhanced giving rise to decreasing of bending modulus and consequently to increasing of undulations.

Recently an anomalous increase in repeat distance of fully hydrated multilayer membranes from DMPC near phase transition temperature was observed [1, 2]. Such behavior was explained by increasing of intermembrane distance due to enlarged undulation repulsion near the critical point. However this can be argued by alternative possibility of increase in lipid bilayer thickness in intermediate region [3, 4].

We performed simultaneous measurements of temperature dependencies of both multilayer repeat distance and lipid bilayer thickness by small-angle neutron scattering. Experiments were held on small angle instrument YuMO of pulsed reactor IBR-2. Single lipid vesicles were obtained by extrusion of multilayer vesicles through filter with 100 nm pore size. [5]. Temperature was raised by successive steps 0.2°C, temperature fluctuations do not exceed 0.05°C. Repeat distance was determined from diffraction peak and bilayer thickness was obtained from radius of gyration as described in [6]. Intermembrane distance was calculated as difference between repeat distance and bilayer thickness. Results are shown in Fig.1. It can be seen from this figure that it is the increase in intermembrane distance which is responsible for the anomalous increase in repeat distance near the chain-melting phase transition temperature. This supports the hypothesis on decreasing of membrane bending modulus due to the enhanced in-plane density fluctuations in the vicinity of critical point.

References

1. T.Honger, K.Mortensen, J.H.Ipsen, J.Lemmich, R.Bauer, O.G.Mouritsen, *Phys. Rev. Lett.*, (**1994**), 72(24), 3911-3914;

2.J.Lemmich, J.H.Ipsen, T.Honger, K.Jorgensen, O.G.Mouritsen, *Modern Phys. Lett. B*, (**1994**), 8(29), 1803-1814;

3.R.Zhang, W.Sun, S. Tristram-Nagle, R.L.Headrick, R.M.Suter, J.F.Nagle, *Phys. Rev. Lett.*, (**1995**), 74(14), 2832-2835;

4.J.Lemmich, K.Mortensen, J.H.Ipsen, T.Honger, R.Bauer, O.G.Mouritsen, *Phys. Rev. Lett.*, (**1995**), 75(21), 3958-3961;

5.R.C. MacDonald, et al, *BBA*, (**1991**), 1061, 297-303;

6.V.I.Gordeliy, L.V.Golubchikova, A.Kuklin, A.G.Syrykh, A.Watts, *Progr. Colloid Polym. Sci.*, (**1993**), 93, 252-256;

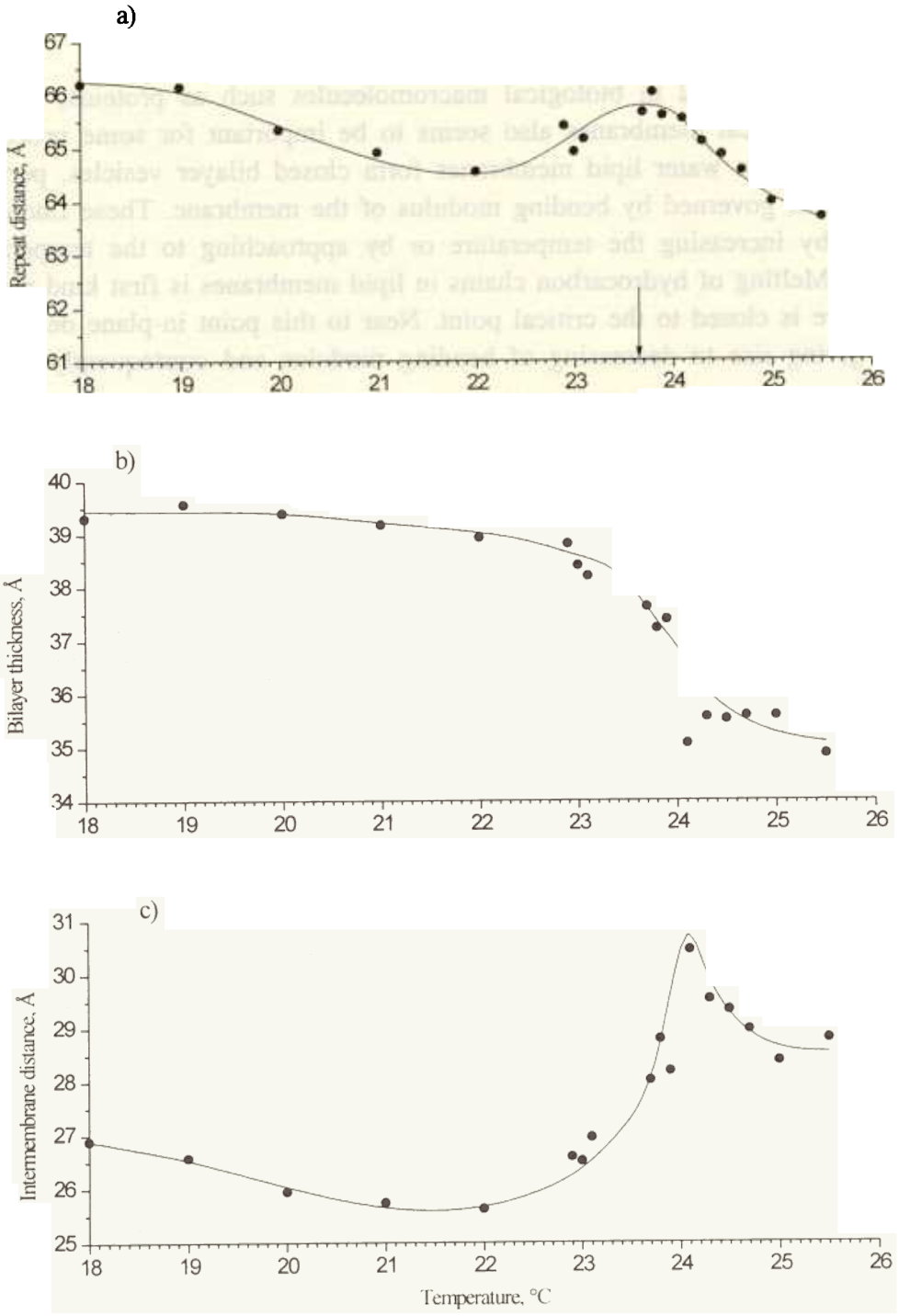

Fig.1. Temperature dependencies of a) multilayer repeat distance, b) lipid bilayer thickness and c) intermembrane distance for lipid membranes from dymiristoyl-phosphatidylcholine

Neutron Spectroscopy of C_{60} Fullerite Hydrogenated under High Pressure

A.I.Kolesnikov[1], V.E.Antonov[1], I.O.Bashkin[1], G.Grosse[3], A.P.Moravsky[2], E.G.Ponyatovsky[2] and F.E.Wagner[3]

[1] Institute of Solid State Physics, Russian Academy of Sciences, 142432 Chernogolovka, Moscow district, Russia

[2] Institute of Chemical Physics in Chernogolovka, Russian Academyof Sciences, 142432 Chernogolovka, Moscow district, Russia

[3] Physics Department, Technical University of Munich, D-85747 Garching, Germany

The inelastic neutron scattering spectra were measured at 85 K for the sample of hydrofullerite quenched after a synthesis at 620 K under a hydrogen pressure of 0.6 GPa, and then for the same sample with a hydrogen content decreased by 1.4 hydrogen molecules per C_{60} molecule after a 35 h annealing at 300 K.

Pure C_{60} fullerite has simple cubic lattice at ambient pressure and T≤255 K [1]. The lattice type changed on hydrogenation. According to the neutron and X-ray diffraction data [2], the $C_{60}H_x$ molecules of both quenched and annealed samples of hydrofullerites at T=85 K formed a *bcc* lattice with the lattice parameters of about 12.00 and 11.72 Å, respectively. The colour, crystal structure, and lattice parameter of the annealed sample agree with the earlier data for $C_{60}H_{36}$ [3]. The lattice contraction observed on annealing at 300~K indicates that hydrogen released from certain lattice sites rather than from bubbles in the crystal.

The sample measured by INS was collected of a few pellets and weighed 0.62 g. The quenched sample was measured first, then annealed at 300~K for 35~h and measured again. The background was determined in a separate empty can measurement and subtracted from the experimental data. The data were transformed to the G(ω) spectra of generalized vibrational density of states versus energy transfer.

Fig.1 shows the G(ω) spectra both of quenched and anneled sample states together with the spectrum of a 3.2 g sample of pure C_{60} measured at 77K.

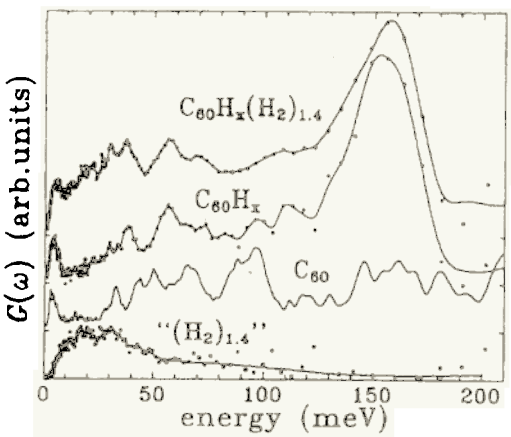

Fig.1 *The generalized vibrational density of states of 'quenched' $C_{60}H_x(H_2)_{1.4}$ and 'annealed' $C_{60}H_x$ samples measured at 85 K, the difference "$(H_2)_{1.4}$" between these two spectra which represents vibrations of interstitial molecular hydrogen in the quenched hydrofullerite, and the spectrum of pure C_{60}, measured at 77 K*

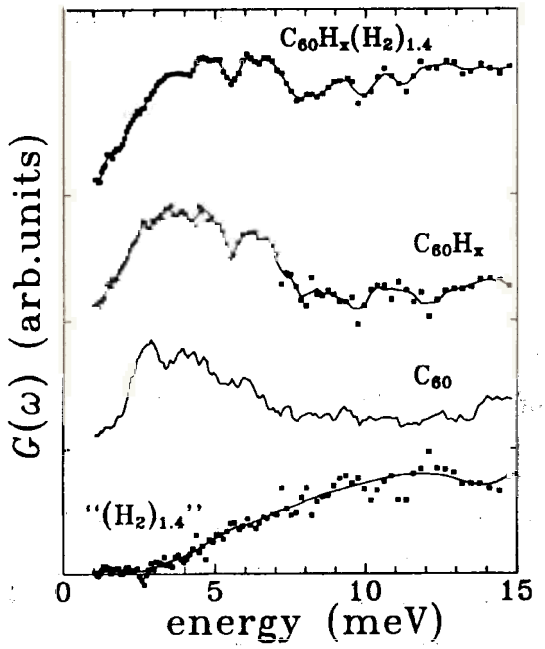

Fig.2 *The same as in figure 1, in the neutron energy transfer range 0-15 meV*

The sprectra of the annealed sample and pure C_{60} are much similar in the range 0-8 meV of intermolecular vibrations. Fig.2 provides the better evidence of it. This indicates that H atoms in the annealed $C_{60}H_x$ sample are chemically bound to C_{60} cages. An astimation from the areas under the G(ω) curves for the anneled $C_{60}H_x$ and pure C_{60} in the region below 8meV gave a correct value of x≅24.

In the range 25-110 meV of radial intramolecular modes in pure C_{60}, the spectra of the hydrofullerites exhibit peaks at 30, 38,56 and 70 meV. Compared to pure C_{60}, the peaks are drastically shifted in energy and have different relative intensities. This means that hydrogen strongly affects the intramolecular C-C interaction. At ω > 110 meV, one largebroad peak centered at ω≈155 meV is observed in the spectra of both $C_{60}H_x$ samples. Folloving the spectrum interpretation for hydrogenated amorphous carbon [4] we attribute this peak to C-H bending modes.

The difference between the spectra of quenched and annealed hydrofulleriets (Fig.1,2, bottom and fig 3) is quite anlike tree other spectra. The difference spectrum is evidentently due to "excess" 2.8 H atoms per C_{60} in the quenched sample. The observed dissimilarity together with the lattice contraction on annealing suggest that these H atoms are not chemically bound to the C_{60} cages and occupy interstitial in the *bcc* $C_{60}H_{24}$ lattice.

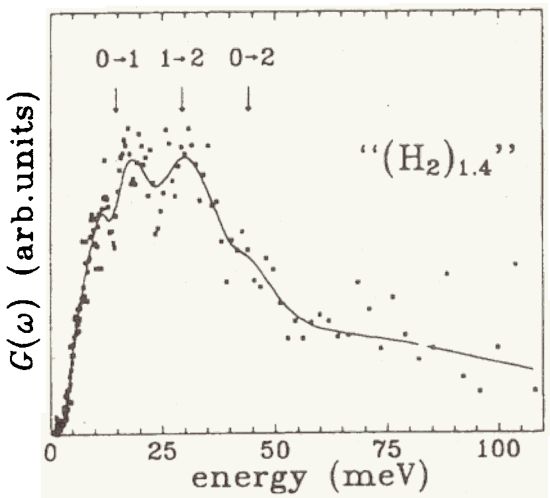

Fig.3 *The difference spectrum from Fig.1 represented on a larger scale. The arrows shows transition energies between rotation states of a free hydrogen molecule with the given rotation quantum numbers.*

As seen from Fig.3, the peaks in the difference spectrum at 12,18.30 and 45 meV can be reasonably well explained whithin the rotator model of molecular hydrogen [5]. The model energy states are given by $E(J)=B\cdot J(J+1)$, where B=7.35

meV and J is the rotational quantum number. The peaks at 30 and 45 meV agree with the (1→2) and (0→2) transitions. The latter has low intensity because it corresponds to the transition between two rotational states in parahydrogen molecules which are coherent neutron scatterers [5]. Two peaks at 12 and 18 meV are assumed to result from splitting of the (0→1) at 14.7 meV due to interaction between H_2 and nearby $C_{60}H_{24}$ molecules. Similar splitting of the (0→1) peak to a pair of peaks at 12.5 and 16 meV was observed ealier in the INS spectrum ofmolecular H_2 trapped in amorphous carbon [4]

1. Heiney P.A. et al 1992, Phys. Rev.B **45**, pp 4544-7
2. Kolesnikov A.I., Antonov V.E., Bashkin I.O., Cornell K., Moravsky A.P., Ponyatovsky E.G., and Wipf H., to be published
3. Hall L.E. et al, 1993 J.Phys.Chem., **97**, pp.5741-4
4. P.J.R.Honebone et al Chem.Phys.Lett. **180**, p.145 (1991)
5. L.D.Landau and E.M.Lifshitz, Quantum Mechanics (Oxford: Pergamon Press, 1965), p.616.

NEUTRON SCATTERING INVESTIGATION OF ICE UNDER HYDROSTATIC HELIUM PRESSURE

I. Natkaniec*&, G.G. Malenkov@, L.S. Smirnov*, L. Bobrowicz#, S.I. Bragin*

*-Frank Laboratory of Neutron Physics, JINR, 141980 Dubna, Russia.
&-H. Niewodniczanski Institute of Nuclear Physics, 31-342 Krakow, Poland.
@-Institute of Physical Chemistry of Russian Ac. Sciences, 117915 Moscow, Russia.
#-Institute of Physics, A. Mickiewicz University, 60-780 Poznan, Poland.

Hydrogen bounded networks formed by water molecules in clathrate hydrates are stabilised by guest molecules and a direct comparison of filled and empty structures is not possible [1]. A remarkable exception is the clathrate-like phase of (H_2O+He), whose p-T phase diagram and crystal structure were recently studied [2,3]. Atoms of He can be enclosed in cavities of the ice II water molecule network without considerable change in its geometry. The He content - x, where x is the fraction of occupied cavities, varies with pressure and the phase is stable when P>2.8 kbar (x=0.62) [3]. The crystal structure of helium clathrate is close to that of ice II and is also orientationally ordered.

Our investigation of the water dynamics in the (H_2O+He) system were performed with the help of the GCA-10 gas compressor used for neutron scattering studies of condensed matter under high pressure [4]. Inelastic incoherent neutron scattering (IINS) spectra of (H_2O+He) system were measured on the NERA-PR spectrometer [5] at a helium pressure of ca. 1 and 3 kbar for different temperatures. The IINS spectra obtained at 1 kbar of helium pressure at 270 K and 236 K correspond to liquid water and ice Ih, respectively. Then the pressure of the helium gas was increased at 270 K up to 3.28 kbar. The subsequent IINS spectra obtained at the following temperatures: 271-270 K, 256-253 K, 253-249 K, 249-239 K, 239-236 K, 236-235 K and 115-114 K, indicate the freezing temperature of the (H_2O+He) system at ca. 239 K. At cooling, the helium pressure was stabilised at ca. 3 kbar. The IINS spectra of H_2O and (H_2O+He) at P=3 kbar close to freezing temperatures are presented in Fig. 1. One can see that the water compressed by helium gas at ca. 3 kbar does not freeze to ice III at ca. 255 K but remains in a liquid state down to ca. 239 K.

The phonon density of states G(E) obtained from the IINS spectra of (H_2O+He) in the solid phases at P=1 kbar and T=236 K and at P=3 kbar and temperatures of 236 and 115 K, respectively, are presented in Fig. 2. One may conclude that the G(E) spectrum of (H_2O+He) at 1 kbar and T=236 K corresponds to ice Ih. The G(E) spectrum of (H_2O+He) at 3 kbar and T=236 K is similar to the G(E) of ice II and this similarity enhances with decreasing temperature, as one may see in Fig. 3. The G(E) spectra obtained at the same pressure for ice III at 250 K and (H_2O+He) at 236 K are also presented in Fig. 3.

References:

1. G.G. Malenkov, Zh. Struct.Khimii, **3** (1962) 220.
2. D. Londono, W.F. Kuhs, J.L. Finney, Nature, **332** (1988) 141.
3. D. Londono, J.L. Finney, W.F. Kuhs, J. Chem. Phys., **97** (1990) 547.
4. S. Habrylo, S.I. Bragin, J. Brankowski, K. Zawalski, W. Iwanski, J. Mayer, W. Nawrocik, I. Natkaniec, PTE, **5** (1989) 63.
5. I. Natkaniec, S.I. Bragin, J. Brankowski, J. Mayer, Proc. ICANS-XII, Abingdon 1993, RAL Report 94-025, Vol. I. p.89-96.

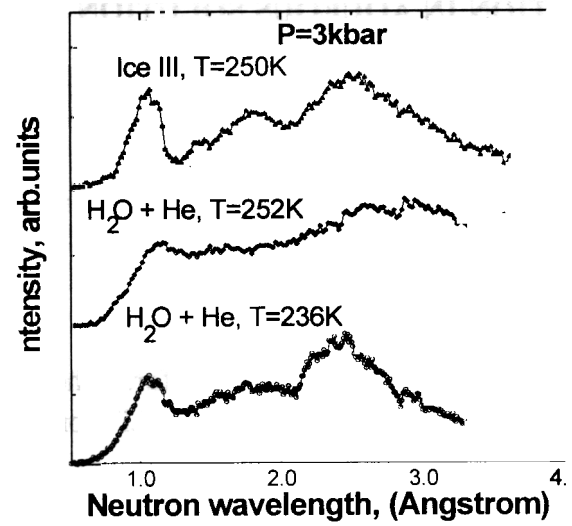

Fig. 1
Comparison of IINS spectra at a hydrostatic pressure of P=3 kbar for ice III at 250 K with a liquid and solid (H_2O+He) mixture close to the freezing temperature at 239 K.

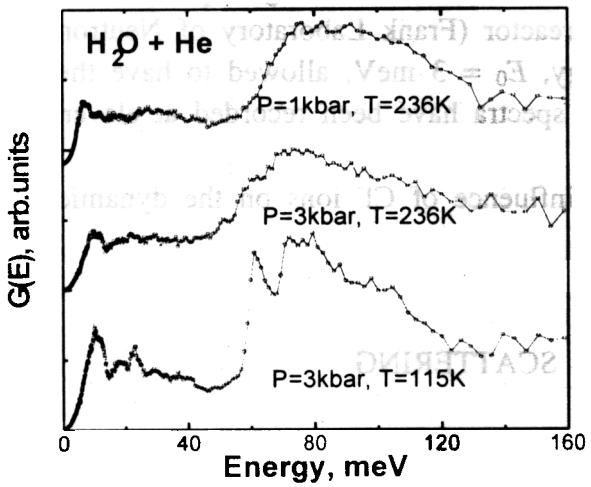

Fig. 2.
Pressure and temperature dependence of the G(E) weighted density of vibrational spectra of (H_2O+He) ices.
At 1 kbar, the G(E) spectrum of (H_2O+He) ice corresponds to the G(E) spectrum of ice Ih, while at 3 kbar these spectra are similar to the corresponding spectra of ice II.

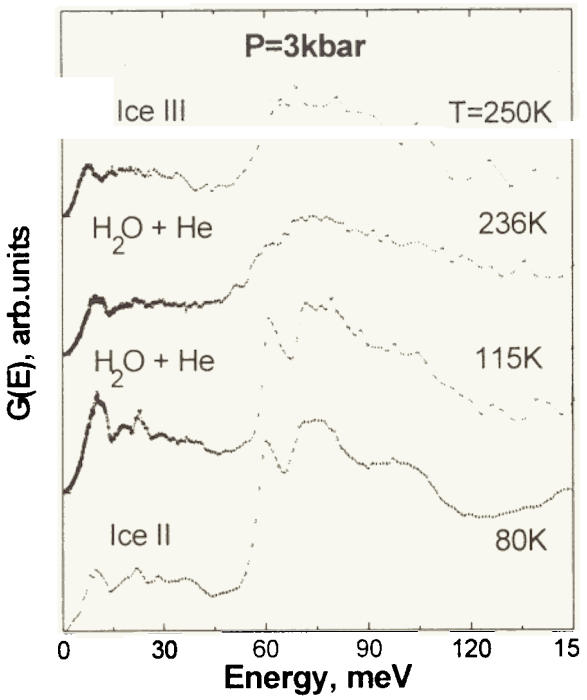

Fig. 3.
Comparison of the G(E) spectra for (H_2O+He) ice under hydrostatic helium pressure of 3 kbar with the corresponding spectra of ice III and ice II compressed in the cylinder-piston high pressure cell at similar temperatures

THE INVESTIGATION OF IONIC HYDRATION IN AQUEOUS SOLUTION OF LICL BY INELASTIC NEUTRON SCATTERING

A.G.Novikov[a], M.N.Rodnikova[b], V.V.Savostin[a] and O.V.Sobolev[a]
[a]State Scientific Centre - Institute of Physics and Power Engineering, 249020, Obninsk, Kaluga Region, Russia
[b]Kurnakov Institute of General and Inorganic Chemistry, Russian Academy of Science, 117907, Moscow, Russia

The aim of this work: using inelastic neutron scattering method, to perform the analysis of diffusion and vibration-rotation motions of water molecules hydrating Li^+ ion in comparison with pure water molecules.

The experiment has been performed on 2M lithium chloride solution and on pure water. It has been carried out with the use of DIN-2PI double time-of-flight spectrometer operating on a neutron beam of the IBR-2 pulsed reactor (Frank Laboratory of Neutron Physics, JINR, Dubna)[1]. The initial neutron energy, E_0 = 3 meV, allowed to have the resolution, ΔE_0 = 0.14 meV. The neutron scattered spectra have been recorded at eleven angles in the range from 11° to 134°.

In the course of data processing we supposed the influence of Cl^- ions on the dynamic properties of water molecules could be neglected [2].

RESULTS: QUASI-ELASTIC SCATTERING

To get the results, concerning with quasi-elastic scattering, the following steps have been done:

– from the total $S(Q,\varepsilon)$ the effects of multiple and inelastic scattering have been removed.

– the experimental quasi-elastic scattering law, $S_{q.el}(Q,\varepsilon)$, obtained for Θ = const. by interpolation procedure has been transformed into the form for Q = const;

- $S_{q.el}(Q,\varepsilon)$ for solution studied was approximated by superposition of two lorentzians [3]:

$$S_{q.el}(Q,\varepsilon) = \frac{1}{\pi}\left[\frac{\alpha\Delta E_1/2}{(\Delta E_1/2)^2+\varepsilon^2}+\frac{(1-\alpha)\Delta E_2/2}{(\Delta E_2/2)^2+\varepsilon^2}\right]\otimes R(Q,\varepsilon) \quad (1$$

where: ΔE_i are the FWHWs of the Lorentzians corresponding to the scattering on the molecules of hydration and bulk water, α - the share of hydration molecules in solution; $R(Q,\varepsilon)$ is the spectrometer resolution function. Sign $\otimes$ means the convolution operation.

For the analysis of the FWHM of the $S_{q.el}(Q,\varepsilon)$ natural line the model of mixed diffusion [4] has been used:

$$\Delta E(Q^2) = \frac{2\hbar}{\tau_0}\,\frac{1+D_0Q^2\tau_0}{1+(D-D_0)Q^2\tau_0}\,\frac{\exp(-2W)}{} \quad (2)$$

Here,τ_0 - residence time, D_0 is the coefficient of continuous (collective) diffusion, D is the total coefficient of self-diffusion, exp(-2W) is Debye-Waller factor $2W = \overline{u^2}Q^2$ where $\overline{u^2}$ is the mean-square amplitude of molecular vibrations.

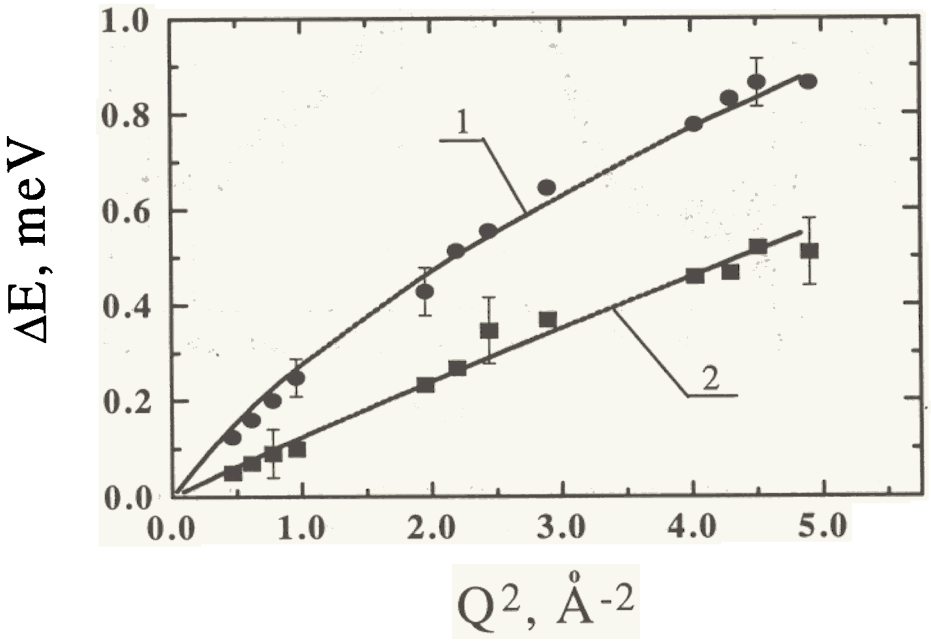

Fig.1. The FWHM of quasi-elastic scattering law natural line for pure water (one lorentzian approximation)and LiCl solution (two-lorentzian approximation).1 - the experimental FWHM for pure water (description by model (3)); ● - the experimental FWHM for bulk water; ■ - and 2 - the experimental FWHM for hydration water and its description by model (3).

The experimental FWHMS for pure water (one lorentzian approximation) and for solution (two lorentzian approximation) are shown on Fig. 1.

For FWHM of pure water model (2) gives following parameters: D = (2.2 ± 0.1)×10^{-5} cm^2/s, D_0 = (0.8 ± 0.05)×10^{-5} cm^2/s, τ_0 = 3.1 ± 0.5 ps.

For FWHM of hydrated water these parameters are: D^{hyd}= (0.95 ± 0.05)×10^{-5} cm^2/s, D_0^{hyd}= (0.79 ± 0.05)×10^{-5} cm^2/s, τ_0^{hyd}=25 ± 10ps.

The D_0^{hyd} obtained is equal to $D_{ion} \approx 0.8\times10^{-5} cm^2/s$ achieved in [5]. τ_0^{hyd} is in agreement with the results of Hertz ($\tau^R \geq$ 20ps [5]).

The share of hydration lorentzian in the common square under quasi-elastic peak $\alpha \approx 0.15 \pm 0.05$ corresponds to four molecules in hydration shell of Li^+ ion.

RESULTS: INELASTIC SCATTERING

The analysis of the inelastic component of $S(Q,\omega)$ has been aimed to get the generalized frequency distribution (GFD) of proton for water molecules in pure water and solution studied.

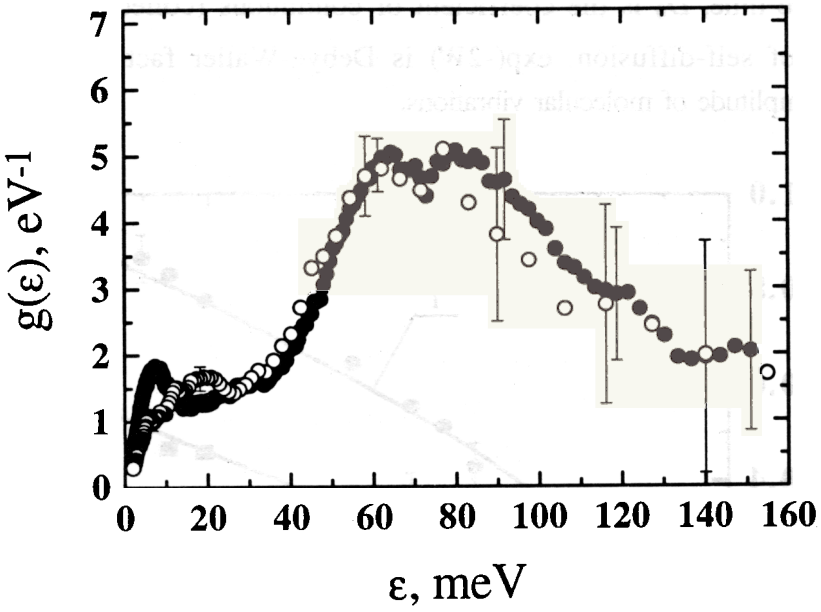

Fig. 2. Generalized frequency distribution of water molecules.
●- pure water; ○- hydration water of Li^+ ion

The procedure of GFD extraction for hydration molecules from inelastic neutron scattering experiment data involved following steps:

- the double-differential scattering cross-section (DDSCS) of pure water has been subtracted from DDSCS of solution. The first has been taken with the weight equal to the relative fraction of bulk water molecules in 2M solution, determined during the analysis of quasi-elastic component of solution studied ($\eta \approx 0.85$). So we get the DDSCS of hydration water.
- the GFD for hydration water has been extracted from its DDSCS obtained above. The method we used for this purpose has been developed and tested on pure water (details and corresponding formulas see in [6]).

Fig. 2 presents the final GFD's we got for pure water and hydration water. GFD extracted corresponds to the region of intermolecular interactions for water molecules ($2meV<\varepsilon<175meV$), and it does not include diffusion and intramolecular degrees of freedom.

As follows from Fig. 2:

- the intensity of the firs translation mode (with the location about $\varepsilon_0 \approx 6$ - 7 meV) corresponding to bending of the O-O-O angle is decreased more than twice;
- the intensity of the second translation mode ($\varepsilon_0 \approx 20meV$) assumed to be connected with H-bonds stretching is increased.
- the libration region of GFD (with maximum at $\varepsilon_0 \approx 60meV$) within the limits of experimental errors we consider as un-changed one.

REFERENCES

1. User Guide. Neutron Experimental Facilities at JINR, ed. Yu.V. Taran. Dubna:JINR Press, 1992.

2. J.Enderby and G.Neilson, Rep. Prog. Phys. 44 (1981) 593.

3. P.S. Salmon, J. Phys. C. 20 (1987) 1573.

4. V.S. Oskotskii, Fiz. Tverd. Tela. 5 (1963) 1082.

5.H.G Hertz, R. Tutsch and H Versmold, Ber.Bunsen.Phys.Chem. 75 (1971).1177.

6. A.G.Novikov, Yu.V.Lisichkin, and N.K.Fomichev, Russian J. Phys. Chem. 60 (1986) 1337.

LATTICE AND METHYL GROUPS DYNAMICS IN SOLID *p*-XYLENE WITH DIFFERENT DEUTERATED MOLECULES

I. Natkaniec[a#], J. Kalus[b], W. Griessl[b], K. Holderna-Natkaniec[c].

[a] - *Frank Laboratory of Neutron Physics, JINR, 141980 Dubna, Russia,*
#- on leave from: H. Niewodniczanski Institute of Nuclear Physics, 31-342 Krakow, Poland.
[b] - *Institute of Physics, University of Bayreuth, 95440 Bayreuth, Germany.*
[c] - *Institute of Physics, A. Mickiewicz University, 61-614 Poznan, Poland.*

Solid *p*-xylene, $C_6H_4(CH_3)_2$, provides a relatively simple example of methyl group rotation within a weak potential caused mainly by intermolecular interaction. This kind of interaction also determines the lattice dynamics. The experimental and calculated phonon density of states G(E) for protonated *p*-xylene are presented in Fig. 1. The lattice dynamics model, based on the"6-exp" atom-atom potential set of parameters fitted to the lattice dynamics of solid benzene [1], can not satisfactorily explain the dynamics of the *p*-xylene crystal. The modified set of potential parameters reproduce the experimental amplitude weighted phonon density of state G(E), quite well, what allow one to study the coupling of the internal methyl rotation with the lattice modes [2].

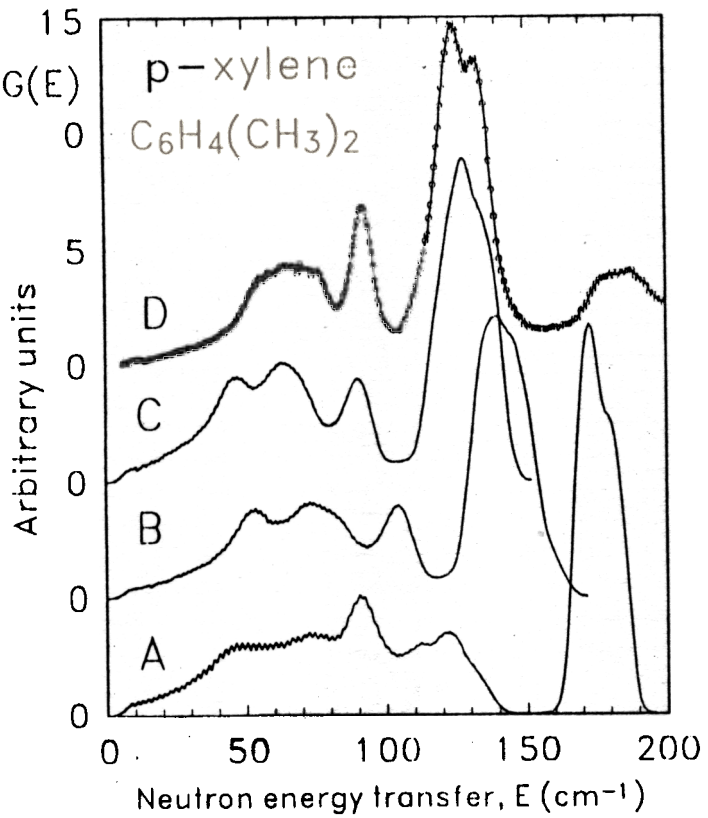

Fig. 1. The calculated amplitude weighted phonon density of states G(E) for protonated p-xylene, covoluted with the resolution of the NERA-PR spectrometer:
A - using the Williams IV(a) set of atom-atom potential parameters fitted to the lattice dynamics of solid benzene [1].
B - using the Williams IV(a) set of parameters, renormalized to the experimental structure [3] of the deuterated p-xylene at 10 K.
C - using a modified set of parameters for the hydrogen atoms of the methyl groups [2].
D - the experimental G(E), obtained from the IINS spectrum of p-xylene measured on the NERA-PR spectrometer at 10 K.

We recently investigated the IINS spectra of solid *p*-xylene with differently deuterated molecules: *p*-xylene-D4 = $C_6D_4(CH_3)_2$, -D6 = $C_6H_4(CD_3)_2$ and -D10 = $C_6D_4(CD_3)_2$. These deuterations change the frequencies of the methyl and lattice vibrations in different ways. This allowed us to test the model of atom-atom potentials in more detail for its usefulness in determining the rotational dynamics of methyl groups. The IINS measurements were performed at 10K in a

neutron energy-loss mode using the NERA-PR inverted geometry multicrystal spectrometer [4] at the IBR-2 high flux pulsed reactor. The IINS spectra measured for 14 scattering angles between 20 and 160 degrees were transformed into the amplitude weighted phonon density of state G(E) using a one phonon scattering approximation. The calculated and experimental G(E) spectra for differently deuterated *p*-xylene molecules are compared in Fig. 2.

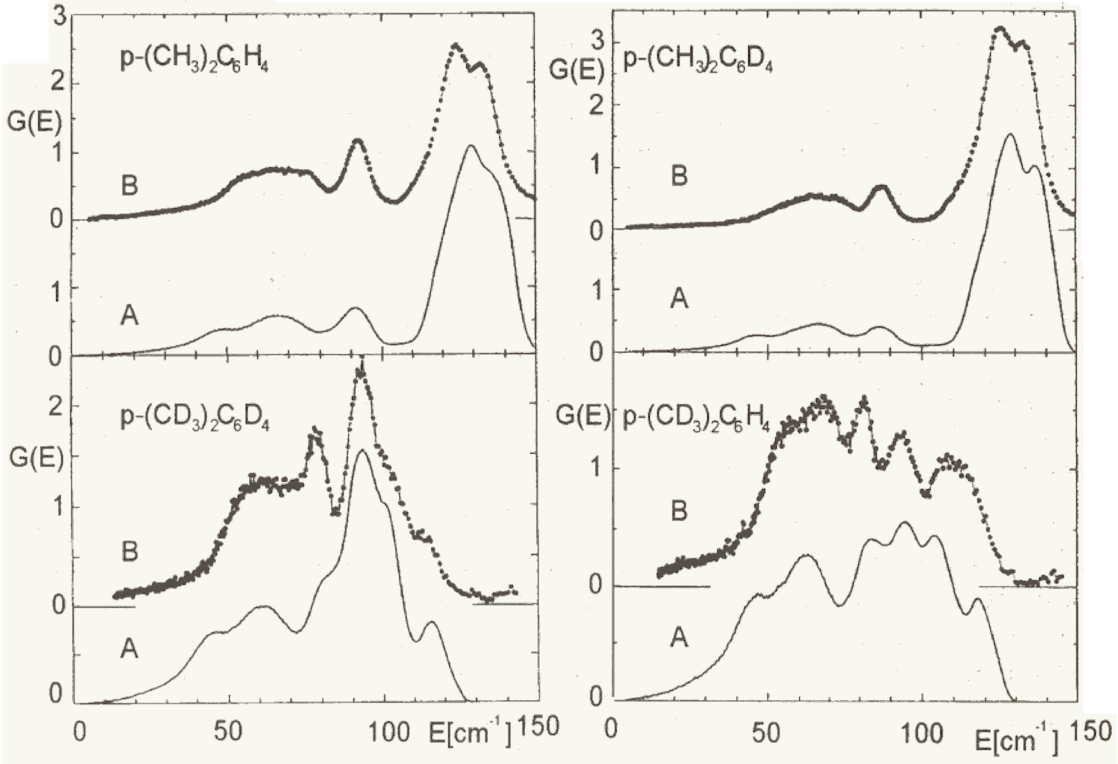

Fig.2. The calculated (A) and experimental (B) amplitude weighted phonon density of states G(E) of solid p-xylene at 10K for differently deuterated molecules.

From the results presented in Fig 2. one can conclude that atom-atom potentials satisfactorily reproduce the modifications in the lattice dynamics and internal rotation of the methyl groups caused by deuteration. By decreasing the potential depth for the H or D atoms of the methyl groups with their neighbouring atoms, we are able to obtain, for one set of potential parameters, the correct energies for the torsional vibrations and to show how they are coupled to the lattice modes. However, this procedure weakens the direct molecule-molecule interaction. The calculated cut-off frequencies of the acoustic translational phonons, at ca. 45cm^{-1}, are lower than their experimental value of ca. 60 cm^{-1}. Thus, the atom-atom potential model has rather limited applications in the study of low-frequency rotational dynamics of molecular groups in crystals.

[1]. G. Tadei, H. Bonadeo, M.P. Marzocchi, S. Califano, J. Chem. Phys., **58** (1973) 966.

[2]. J. Kalus, M. Monkenbush, I. Natkaniec, M. Prager, J. Wolfrum, F.Worlen, Mol. Cryst. Liq. Cryst., **268** (1995) 1-20.

[3]. M. Prager, W.I.F. David, R.M. Ibberson, J. Chem. Phys., **95** (1991) 2473.

[4]. I. Natkaniec, S.I. Bragin, J. Brankowski, J. Mayer, Proc. ICANS XII, Abingdon 1993, RAL Report 94-025, Vol. I. p.89-96.

Phonon dispersion curves in Fe-18Cr-10Mn-15Ni FCC steel

S.A.Danilkin [a], *E.L.Yadrowski*

[a] Institute of Physics and Power Engineering, Obninsk, Russia

Austenitic Fe-Cr-Mn(Ni) alloys are of interest because interstitial nitrogen stabilizes the FCC structure and improves the strength, toughness and corrosion resistance. The Nitrogen effect on the interatomic interactions in austenitic steel was studied earlier for polycrystalline samples by inelastic neutron scattering [1]. To obtain detailed information on the force constants, measurements with single crystals are necessary to be conducted. So far the difficulty was to producing large single crystals of nitrogen austenitic steel.

Phonon dispersion curve measurements were started with an austenitic Fe-18Cr-10Mn-15Ni steel single crystal containing no nitrogen additions. First, the lattice parameter was measured. For this purpose the chopper in the spectrometer DIN-2PI [2] was removed and the time-of-flight diffraction spectrum of an oriented crystal was measured. The lattice parameter equals a=0.359 nm for the (200) plane at the scattering angle 2Θ=128.87°. The mosaic spread of the crystal was estimated to be as large as 40'. This is commensurable with an angular divergence of the neutron beam.

Dispersion curve measurements were performed with the multidetector spectrometer DIN-2PI. In the measurements, we used the geometry with the wave vector of the scattered neutrons $\boldsymbol{k}$ coinciding with the selected symmetry direction which does not pass through the origin of the reciprocal space. With this method, we measure phonons with a wave vector in the desired symmetry direction for the selected scattering angle Θ. The value of $\boldsymbol{k}_0$ and the crystal orientation are defined by the crystal structure and Θ.

For the optimal choice of experimental conditions, we performed model calculations with dispersion curves for a invar alloy $Fe_{0.7}Ni_{0.3}$ of [3]. We performed 13 different scans. The number of phonons measured in one scan varied from 2 to 4, the measuring time was from 2 hours for low frequency phonons to 10 - 12 hours for phonons with $q/q_m \cong 0.5$. In the measurements we used simultaneously 15 - 30 detectors, but for the lattice dynamics analysis only phonons with the wave vectors in the [110] direction were selected.

Figure 1 shows the results obtained for a Fe-18Cr-10Mn-15Ni steel. Only two phonon branches, L and T_1, are shown because for the(100) reciprocal plane $S(\boldsymbol{K},\omega)$=0 for theT_2 branch. The maximum frequencies of the L and T_1 branches are in agreement with the peak positions in the vibrational frequency distribution of the polycrystalline alloy - 23 and 32 meV [1].

The experimental data were analyzed in the frame of the model of lattice dynamics with considering the central force interaction for the first two neighbours [3]. For two measured dispersion branches it is possible to determine the force constants for the first neighbours $a_1=V''(r_1)$ and $b_1=V'(r_1)/r_1$, and the sum of the force constants a_2+b_2 for the second neighbours. The fitting procedure gives the following values: a_1=3.899±0.012, b_1=-0.198±0.008 and a_2+b_2=0.109±0.016 ($\times 10^4$ dyn/cm). To determine a_2 and b_2, additional measurements of the [110] T_2 branch or phonon dispersion in other symmetry directions should be performed.

Figure1 shows that the calculated dispersion curves are in good agreement with the experimental data for the transversal branch T_1 and longitudinal phonons for $q/q_m < 0.4$. The difference for high-energy L-phonons ($\hbar\omega \cong 32$ meV) may be connected with a simplification

of the dynamic model used or the incoherent scattering background. For the alloys studied the incoherent cross section is significant due to the presence of Ni and Cr. Therefore, for this energy region it was difficult to distinguish the peaks due to coherent scattering.

References:

[1] V.G.Gavriliuk, S.A.Danilkin et al., Izvestija RAN, Metalli, 5 (1995) 51.

[2] Neutron experimental facilities at JINR, User Guide, Frank Laboratory of Neutron Physics, Joint Institute for Nuclear Research, Dubna, 1992, p.24.

[3] S.Garg, H.Gupta et al., J.Phys.F, Met. Phys., 15 (1985) 1895.

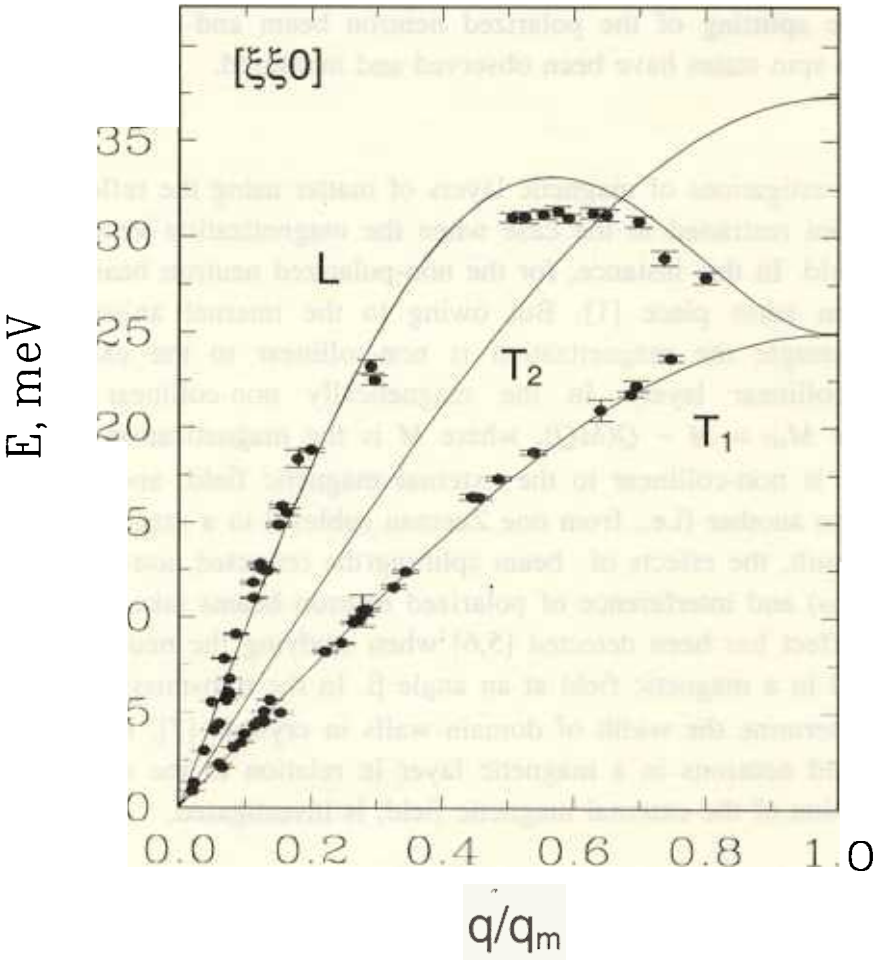

Fig.1. Phonon dispersion curves in a Fe-18Cr-10Mn-15Ni steel. • - experiment; — model.

REFRACTION OF POLARIZED NEUTRONS IN A MAGNETICALLY NON-COLLINEAR LAYER

V.L. Aksenov[a], E.B. Dokukin[a], S.V. Kozhevnikov[a],
Yu.V. Nikitenko[a], A.V. Petrenko[a] and J. Schreiber[b]

Frank Laboratory of Neutron Physics, JINR, 141980 Dubna, Moscow Region, Russia
[b] Fraunhofer Institute for Non-destructive Testing, D-01326 Dresden, Germany

The refraction of polarized neutrons in a magnetic layer in relation to the neutron wavelength, the magnitude and direction of an external magnetic field, has been investigated experimentally. The effects of space splitting of the polarized neutron beam and the interference of neutron beams with different spin states have been observed and measured.

1. Introduction

So far the investigations of magnetic layers of matter using the reflection or transmission of neutrons have been restricted to the case when the magnetization vector is collinear to the external magnetic field. In this instance, for the non-polarized neutron beam in a magnetic layer the double refraction takes place [1]. But owing to the internal anisotropy and the shape anisotropy of the sample the magnetization is non-collinear to the external magnetic field (magnetically non-collinear layer). In the magnetically non-collinear layer the effective magnetization vector $M_{eff} = M - Q(MQ)$, where M is the magnetization vector, and Q is the transfer momentum, is non-collinear to the external magnetic field, and the neutron transition from one spin state to another (i.e., from one Zeeman sublevel in a magnetic field to another) is realized [2]. As a result, the effects of beam splitting(the refracted non-polarized neutron beam splits into four beams) and interference of polarized neutron beams take place [3,4]. At present, the beam splitting effect has been detected [5,6] when studying the neutron reflection from the magnetic film placed in a magnetic field at an angle β. In the transmission geometry this effect has been used to determine the width of domain walls in crystals [7]. In the present paper the refraction of polarized neutrons in a magnetic layer in relation to the neutron wavelength, the magnitude and direction of the external magnetic field, is investigated.

2. Experimental details

The investigations have been conducted at the polarized neutron spectrometer at the IBR-2 reactor. A scheme of a complete polarization analysis [2] has been realized. The angle β between the direction of the magnetic field and the sample plane was set within $0 \div 90°$. The divergence of the neutron beam in the horizontal plane was ± 0.1 mrad, and the grazing angle of the beam incident on the sample was $\theta = 3.17$ mrad. The investigated sample was a magnetic layer produced by evaporation sputtering of FeSiAl(Si-4.4at.%, Al-9.6at.%)on a ceramics substrate($10 \times 20 \times 1 mm^3$). The thickness of the layer was 5μm and the coercivity was 3.5Oe.

3. Results and discussion

Figure 1 presents the integral in wavelength ($1 \div 12$ E) count versus the grazing angle θ_{tr} of the transmitted beam. It is seen from the figure that for $\beta = 70°$ as compared with $\beta = 0°$ a

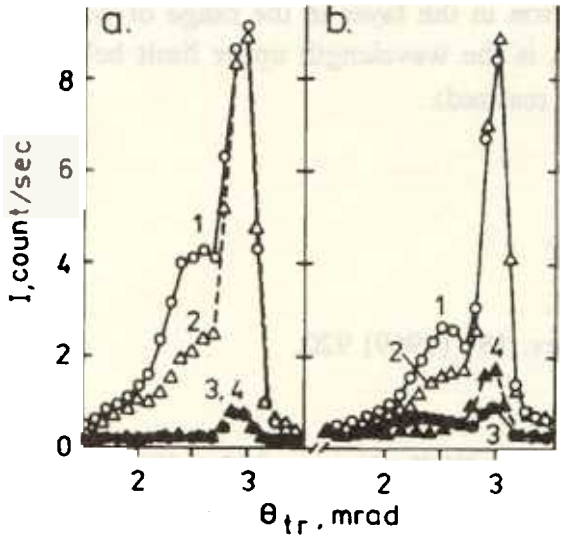

Fig. 1. The dependence of the integral neutron intensity I(count/sec) on the grazing angle θ_{tr} at β=0°(a) and 70°(b) for the "– –"(curve 1), "+ +"(curve 2), "– +"(curve 3), "+ –"(curve 4) beams.

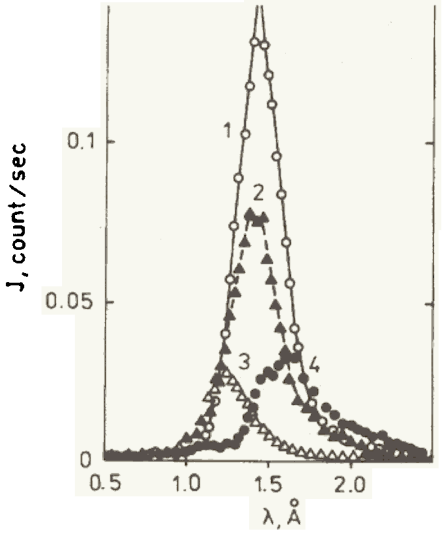

Fig. 2. The spectral dependence of the intensity J(λ) at θ_{tr}=2.8 mrad, β=70° and H=4.6kOe for the "– –"(curve 1), "+ +"(curve 2), "– +"(curve 3), "+ –"(curve 4) beams.

decrease in intensity of the "– –" and "+ +" refracted beams (peaks at the left) can be observed. At the same time, the "+ –" and "– +" beams appear; the first one is on the right of the "– –" beam, and the second is on the left of the "+ +" beam. The distance between the "–+" and "+ –" beams at the detector is 1.4 mm ($\Delta\theta_{tr}$ = 0.535 mrad). This result is interpreted as the observation of the generation of new beams at β≠0. The experimental data is represented as the difference of the squares of the grazing angles of the "+ –" and "– +" beams $\Delta\theta^2 = \theta_{tr,+-}^2 - \theta_{tr,-+}^2$. The observed dependence $\Delta\theta^2(\text{mrad}^2) = \alpha H(\text{kOe})\lambda^2(\text{E}^2)$ (λ is the neutron wavelength, α is the proportionality coefficient) is in agreement with the concept of beam generation associated with the existence of the transition between the Zeeman sublevels in the external magnetic field *H*. For *H*=4.6kOe and 6.8 kOe, however, the α coefficient is 0.23, which is 20% less than the theoretical value $\alpha = 8m\mu/h^2 = 0.294$ (*m* is the neutron mass, μ is the neutron magnetic moment, *h* is the Planck constant). The spectral dependence of the neutron intensity at θ_{tr}=2.8mrad is illustrated in Fig.2. It can be seen that the transmittance for all beams has a maximum at some wavelength values λ_{ij}, where i,j= +, –. $\Delta\lambda^{-2} = (\lambda_{+-}^{-2} - \lambda_{-+}^{-2}) \propto H$ in the range of values *H*=1÷6.8 kOe. The conducted measurements of the transmittance in relation to the angle β in the interval 0÷90° at *H*=4.6 kOe have shown that as β increases the transmittance of the "+ +" and "– –" beams decreases, and the transmittance of the "+ –" and "– +" beams increases. The spectral dependence of the transmittance of the "+ +" beam is presented in Fig.3.

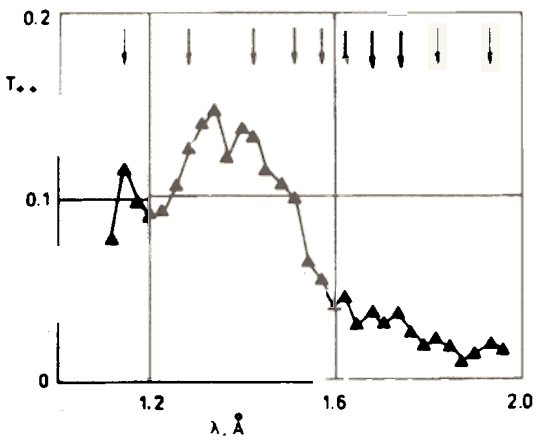

Fig. 3. The spectral dependence of the transmittance $T_{++}(\lambda)$ of the "+ +" beam at θ_{tr}=2.8 mrad, H=6.8kOe and β=70°. The arrows denote the wavelengths at which the transmittance has local maxima.

The transmittance oscillations whose period decreases as the neutron wavelength increases up to λ≈1.6 E can be easily seen. This behaviour is explained by the

interference of the "+" and "-" states of the neutron in the layer in the range of wavelengths from 0 to the boundary wavelength $\lambda_{lim} \approx 1.6$Å ($\lambda_{lim}$ is the wavelength upper limit below which the "+ +" neutron transition on the first interface is realized).

References

[1] D. Hughes, M. Burgy, Phys. Rev. 81 (1951) 498.
[2] R.M. Moon, T. Riste and W.C. Koehler, Phys.Rev. 181 (1969) 920.
[3] V.K. Ignatovich, Letters to JETP 28 (1978) 311.
[4] N.K. Pleshanov, Z.Phys. 94 (1994) 233.
[5] G.P. Felcher, S. Adenwalla, V.O. De Haan, A.A. Van Well, Nature 377 (1995) 409.
[6] D.A. Korneev, V.I. Bodnarchuk, V.K. Ignatovich, Letters to JETP 63 (1996) 900.
[7] O. Schaerpf, Physica Scripta 24 (1988) 58.

Element Depth Profiles of Porous Silicon

A.P.Kobzev, O.A.Nikonov
Frank Laboratory of Neutron Physics, Joint Institute for Nuclear Research, Dubna, Russia

M.Kulik, J. Żuk, H. Krzyżanowska, T.J. Ochalski
Institute of Physics, Maria Curie-Skłodowska University, Lublin, Poland

1. INTRODUCTION

Porous silicon has been a subject of intensive investigations since the initial demonstration of efficient visible photoluminescence in this material by L.T. Canham in 1990 [1].The progress in research on porous Si was reviewed recently [2,3]. Emission from porous Si is completely different from that observed in bulk crystalline Si, where the weak near-infrared luminescence associated with the indirect band gap of 1.1 eV has been known for a long time. For porous silicon, a large „blue" shift of the fundamental absorption edge has been reported. Spectacular optical properties of porous silicon are generally attributed to the spatial confinement of photo-excited carriers in nanometer-sized Si quantum wires or dots [1-3].

There are however, some other mechanisms of light emission in porous silicon. One of them has been linked to the E' centre in SiO_2 (an oxygen vacancy with unpaired electron) and proposed to explain strong blue emission observed in porous silicon, when excited with ultra violet light or protons [4]. It would be interesting therefore, to estimate oxygen content on a large (up to 1000 m^2/cm^3) surface of porous silicon.

2. EXPERIMENT

The samples used in a present experiment were prepared from p-type (111) silicon wafers of 10 Ωcm resistivity. The porous layers were formed by anodization in a 48 % HF-ethyl alcohol solution at a current density of about 20 $mAcm^{-2}$. The technology of preparing porous silicon was described in [4]. The thickness of the porous layer was about 5 μm, as determined by interferometric microscopy.

Both non-destructive nuclear methods ERD (Elastic Recoil Detection) and RBS (Rutherford Backscattering Spectroscopy) have been used in the investigation the depth element profiles in porous silicon. The measurements of RBS and ERD spectra have been carried out at EG-5 accelerator in the Frank Laboratory of Neutron Physics.

In the RBS experiment the detector was positioned at scattering angle 170° with respect incident beam. The surface of sample was tilted to the ion beam at the angle 60°. The detector resolution was 15 keV for 5.5 MeV α-particle. We have overcome the difficulties of the RBS method in the investigations of the concentration of light element (O) along with the heavier (Si) and used in this case the nuclear

reaction $^{16}O(\alpha,\alpha)^{16}O$ to profile oxygen directly [5]. The elastic nuclear resonance at 3.045 MeV is particularly suitable, because it has a large back scattering cross section (17 times greater than for Rutherford scattering) and a width of resonance is about 10 keV . The measurements have been performed in a such way, that the energy of incident beam of ions $^4He^+$ was changed in small increments in the range from 3.04 MeV to 3.20 MeV. The backscattering spectra were collected for everything energies. So the resonance shifted from surface into 5000 nm for highest energy and we had measured the oxygen profile in detail over the range of depth above.

The ERD spectra have been investigated for both porous and crystalline silicon. The 2.5 MeV ^4He ions were incident on a solid target at an angle of 15° with respect to surface of the sample. The scattered $^4He^+$ ions were absorbed in stopper aluminium foil of 9.5μm thickness. In contrary the recoiling nuclei (protons) lost only a part of the full energy and were collected by a detector positioned at an laboratory scattering angle of 30° away from the direction of incidence.

3. RESULTS AND DISCUSSION

The typical spectra of ^4He ions scattered from the sample of porous silicon are presented in Fig.1 for two initial energies. The peak of the resonantly scattered $^4He^+$ particles rides over the background non-resonant scattering from oxygen. This background, in turn, sits on a top of the continuum of the elastic scattering by silicon nuclei in the porous layer of the investigated sample.

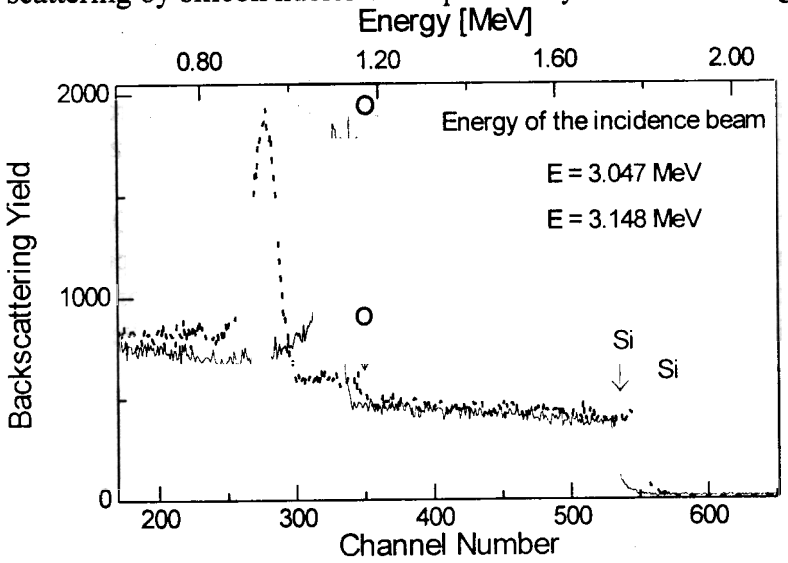

Fig. 1. Spectra of $^4He^+$ backscattered by porous silicon sample.

The peak for 3.047 MeV ^4He ions has more sharp right edge because the resonance entered to the target partially in this case. A shift to depth of the peak of oxygen resonance with increasing the initial energy of bombarding particles is observed since ^4He ions reaches of the resonance energy at the increasing depth . A square of the peak is proportional to an oxygen atom concentration for the given depth.

On the spectra one can see the yield ^4He ions scattered by Si atoms. The background for the spectral regions according to surface layers is absent in this case. The element concentrations are obtained with help a computer code [6] after modelling everything spectra using one joint model of the sample.

The ERD spectra obtained for the crystalline silicon and porous silicon sample are shown in Fig.2 At a spectrum for crystalline silicon one can see the peak near the channel number 460. The yield of this peak is very small, as compared to the one for the porous silicon layer. It means that the hydrogen

atoms present only at the surface of silicon. Since porous silicon has the vast specific surface the yield of the recoiling hydrogen atoms for the porous sample is substantially more than for crystalline and depth profile extends at a whole depth available for the measurement.

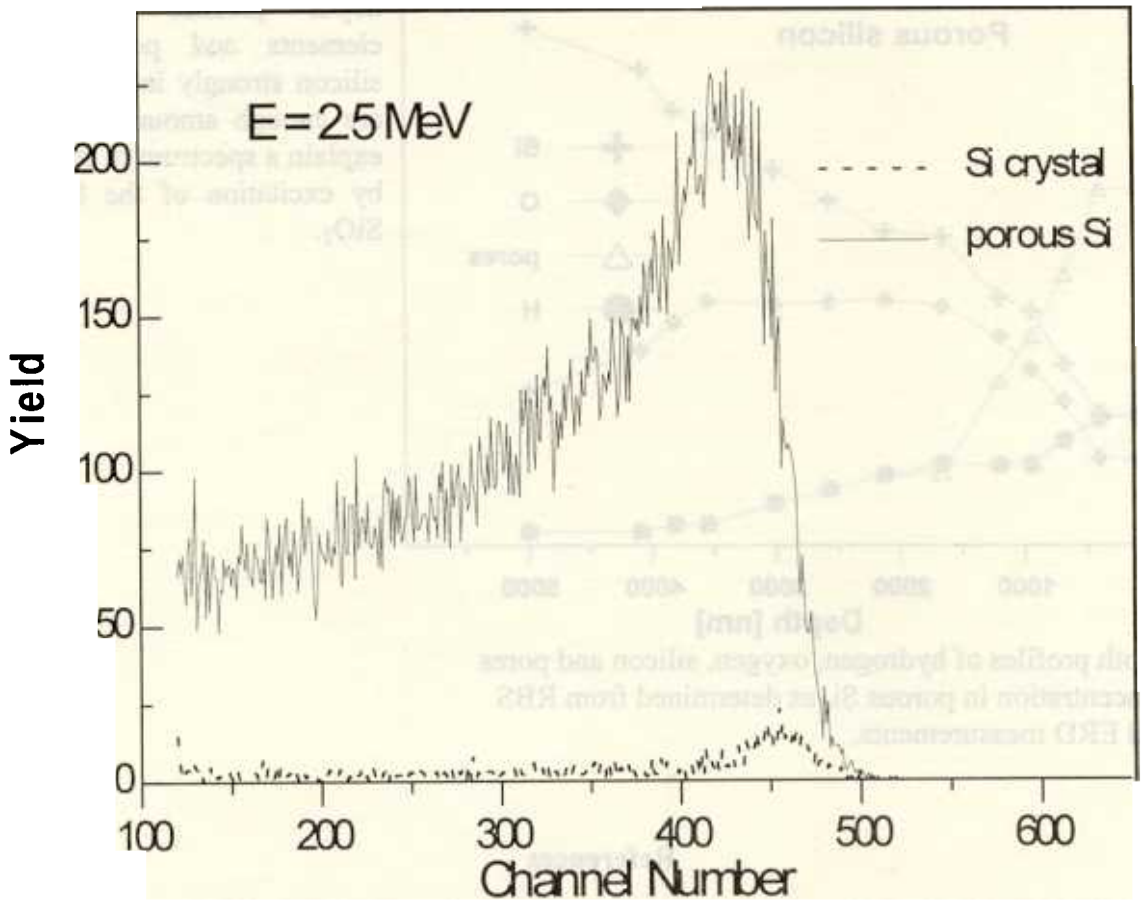

Fig. 2. ERD spectra of porous and crystalline Si

The depth profiles of the different elements and pores in the porous silicon layer were calculated in two steps.. In the first step, the depth profile of hydrogen in the porous silicon was determined on a basis of the ERD spectrum. Than these data were used in the calculations of the depth profiles of other elements (Si,O) and pores by modelling of twelve RBS spectra with the help of a computer code[6]. These results are shown in Fig. 3. A special element was included in the model of a sample what we attributed with the pores. It did not scatter He ions and had very small stopping cross sections. This procedure gives possibility to account the presence the pores in solid with first approximation only.

The concentration of Si atoms is the smallest (~20 %) in the subsurface region and gradually increases with a depth up to 75% (Fig. 3). The porous Si layer is non-homogeneous, with a porosity (after anodization) ranging from about 50 % close to the surface to less than 10 % at a depth of 1600 nm and slowly decreases up to almost zero for the depth 4000 nm. A concentration of oxygen is less than 30% for whole thickness of porous silicon layer. A ratio C_{Si}/C_O increases from 1.2 at surface to 3.2 with

the growth a depth to 5000 nm. Therefore, it can be assumed, that the Si wires in porous silicon are covered with silicon oxide layers. Moreover the hydrogen atoms, which are present in porous silicon after anodization, probably, appear as H_2O.

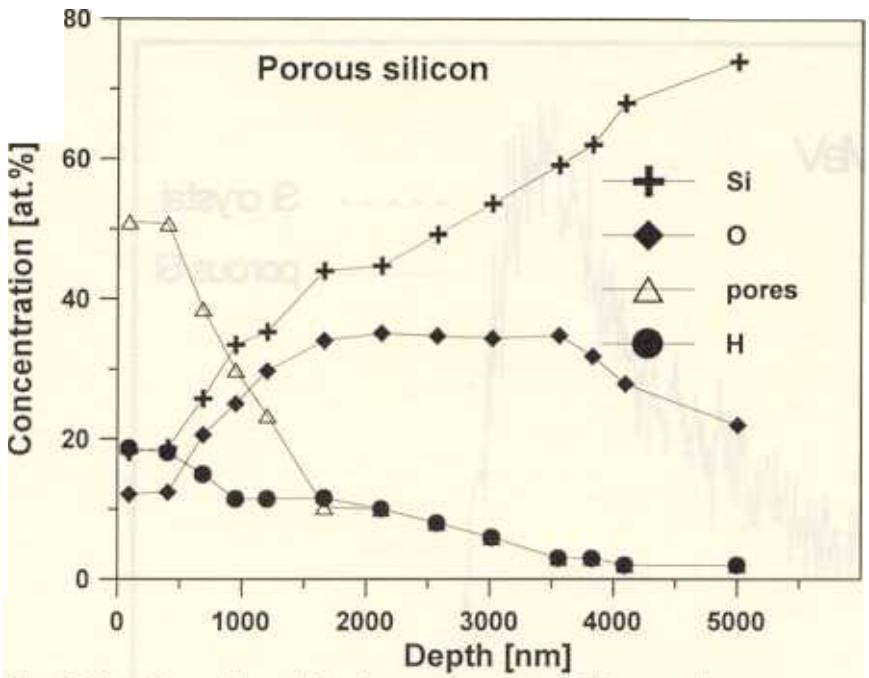

Fig. 3. Depth profiles of hydrogen, oxygen, silicon and pores concentration in porous Si, as determined from RBS and ERD measurements.

So, the performed investigation of depth profiles of everything elements and pores in porous silicon strongly indicate, that there are enough amounts of oxygen to explain a spectrum of luminescence by excitation of the E' centre in SiO_2.

References

1. L.T. Canham. Silicon quantum wire array fabrication by electrochemical and chemical dissolution of wafer. Appl. Phys. Lett. **57** (10),1046 - 1051 (1990).
2. Y. Kanemitsu. Light emission from porous silicon and related materials. Phys. Rep. **263** (1), 1-91 (1995).
3. G.C. John and V.A. Singh. Porous silicon: theoretical studies. Phys. Rep. **263** (2), 93-151 (1995).
4. J.Żuk, R. Kuduk, M. Kulik, J. Liśkiewicz, D. Mączka, P.V. Zhukovski, V.F. Stelmakh, V.P. Bondarenko and A.M. Dorofeev. Ionoluminescence of porous silicon. J. Lumin. **57**, 57-60 (1993).
5. L.P.Chernenko, A.P.Kobzev, D.A.Korneev and D.M.Shirokov. Backscattering methods possibilities for precise determination of oxygen profile in axide films by use of the elastic resonance in reaction $^{16}O(^4He, ^4He)^{16}O$ at 3.045 MeV of ^4He. Surface and Interface Analysis. vol.**18**, 585-588 (1992).
6. V.Bogac and D.M.Shirokov. New computer iterative fitting program DVBS for backscattering analysis. Nucl. Instrum. and Meth. in Phys. Res. **B85**, 264-267 (1994).

EPITHERMAL NAA FOR STUDYING THE ENVIRONMENT

M.V. FRONTASYEVA, E. STEINNES*

Joint Institute for Nuclear Research (JINR), Dubna, Russia
*Norwegian University of Science and Technology, Trondheim, Norway

The advent of analytical techniques for the simultaneous determination of a great number of elements has created an enormous interest for multi-element studies in environmental sciences. Instrumental neutron activation analysis (INAA) has shown to be useful for a number of sample types of interest in environmental studies, and should find more extensive use in this area. Epithermal neutron activation analysis (ENAA) has certain advantages over the conventional INAA for many trace elements in terms of improvement in precision and lowering of detection limits, reduction of high matrix activity and fission interferences if any.

Since Brunfelt and Steinnes [1] reported the first multi-element study on silicate rocks using ENAA, this technique soon became a routine tool in many earth science laboratories. ENAA was early shown to exhibit an excellent multi-element capability in the case of coal and coal fly ash [2].

Two areas of environmental analysis seems to deserve particular attention when the feasibility of ENAA relative to non-nuclear multi-element techniques is to be discussed: the analysis of airborne particulate matter, and the related subject on analysis of biomonitors of atmospheric deposition: Analyses of airborne particulate matter is a case where ENAA should be particularly useful. This is mainly due to the fact that the total mass of the aerosol collected on a filter sample is often rather small, and thus favours direct instrumental techniques rather than those depending on dissolution of the sample prior to analysis. Air filter analysis therefore seems to be an area where INAA hardly can be replaced by any non-nuclear analytical technique at the present state of the art. Comprehensive texts on INAA of airborne particulate matter have appeared in the literature [3, 4]. The elements that form the major activity upon neutron activation of aerosols are very much the same ones as in the case of. silicate rocks and fly ash. This means that the advantages of using epithermal activation should also be similar, provided that the induced activity is sufficient to yield satisfactory counting statistics. As shown by Landsberger [5] this is indeed the case for several trace elements of importance in studies of long range atmospheric transport. In the opinion of the authors this is an area where much remains to be done, and at JINR, Dubna, ENAA is now being used in several projects involving the analysis of aerosol filters. A similar case where ENAA has shown strong performance is in the analysis of mosses used as biomonitors of atmospheric deposition. Mosses have been used in Norway since 1977 on a regular basis to monitor atmospheric deposition of heavy metals in a nation-wide grid. The analytical approach used from the beginning was INAA, supplemented by atomic absorption spectrometry for the elements Pb, Cd, Cu, and Ni. Prior to the survey in 1990 it became evident that ICP-MS, which had then become available, was able to produce results of acceptable quality for all elements of first priority, and has therefore been used since then in the regular monitoring work.

During the same period, work has continued to test the feasibility of other analytical techniques for the trace element determination in moss. In particular the use of ENAA was

investigated employing the IBR-2 pulsed fast reactor in Dubna, which is characterised by a particularly high fraction of resonance and fast neutrons in the total spectrum. By this means the determination of 15 elements (Zr, Sn, Hf, Ta, W, Au, Th, and eight REE) previously not detected in such samples was demonstrated [6], and the relative merits of ENAA and ICP-MS in moss analysis were discussed on the basis of an intercomparison exercise [7]. ICP-MS laboratories are now capable of producing apparently satisfactory results for about 55 elements in mosses. The corresponding figure for ENAA is around 45. In 40 cases both techniques can be used, and for a majority of these elements it is difficult on the basis of present evidence to give preference to one technique or the other. In 7 cases (Sc, As, Sb, Hf, Ta, Au, Th) ENAA is judged to be the preferred technique, whereas ICP-MS seems preferable in 5 cases (Sr, Sn, Ba, Ce, Nd). Four elements (Cl, Br, I, Se) could only be determined well by ENAA, whereas the reverse situation applied for another 14 elements (Li, Cu, Ga,Ge, Y, Cd, Te, Pr, Dy, Ho, Er, Tl, Pb, Bi). The choice of either multi-element technique thus depends on the purpose of the investigation and the priority of elements. It should be added that the simultaneous determination of the halogens Cl, Br and I, which is rather straightforward by ENAA in mosses as well as in several other environmental sample types, is hardly possible at all by any existing non-nuclear technique at the levels concerned.

REFERENCES

1 BRUNFELT, A.O., STEINNES, E., Instrumental activation analysis of silicate rocks with epithermal neutrons, Anal. Chim. Acta **48** (1969) 13-24.

[2] ROWE, J.J.,STEINNES,E., Instrumental activation analysis of coal and fly ash with thermal and epithermal neutrons, J. Radioanal.Nucl. Chem. **37** (1977) 849-856.

[3] ALIAN, A., SANSONI, B., A review on activation analysis of particulate matter, J. Radioanal. Nucl. Chem., **89** (1985) 191-275.

[4] INTERNATIONAL ATOMIC ENERGY AGENCY, Sampling and Analytical Methodologies for INAA of Airborne Particulate Matter, Training Course Series No. 4,Vienna (1992), 56 pp.

[5] LANDSBERGER, S., Improved methodology for the determination of the seven elemental tracer long-distance pollution signatures using thermal and epithermal neutron activation analysis, Anal. Chem. **60** (1988) 1842-1845.

[6] FRONTASYEVA, M.V., NAZAROV, V.M., STEINNES, E., Moss as monitor of heavy metal deposition: Comparison of different multi-element analytical techniques, J. Radioanal. Nucl. Chem. **181** (1994) 363-371.

[7] FRONTASYEVA, M.V., GRASS, F., NAZAROV, V.M., STEINNES, E., Intercomparison of moss reference material by different multi-element techniques, J. Radioanal. Nucl. Chem. **192** (1995) 371-379.

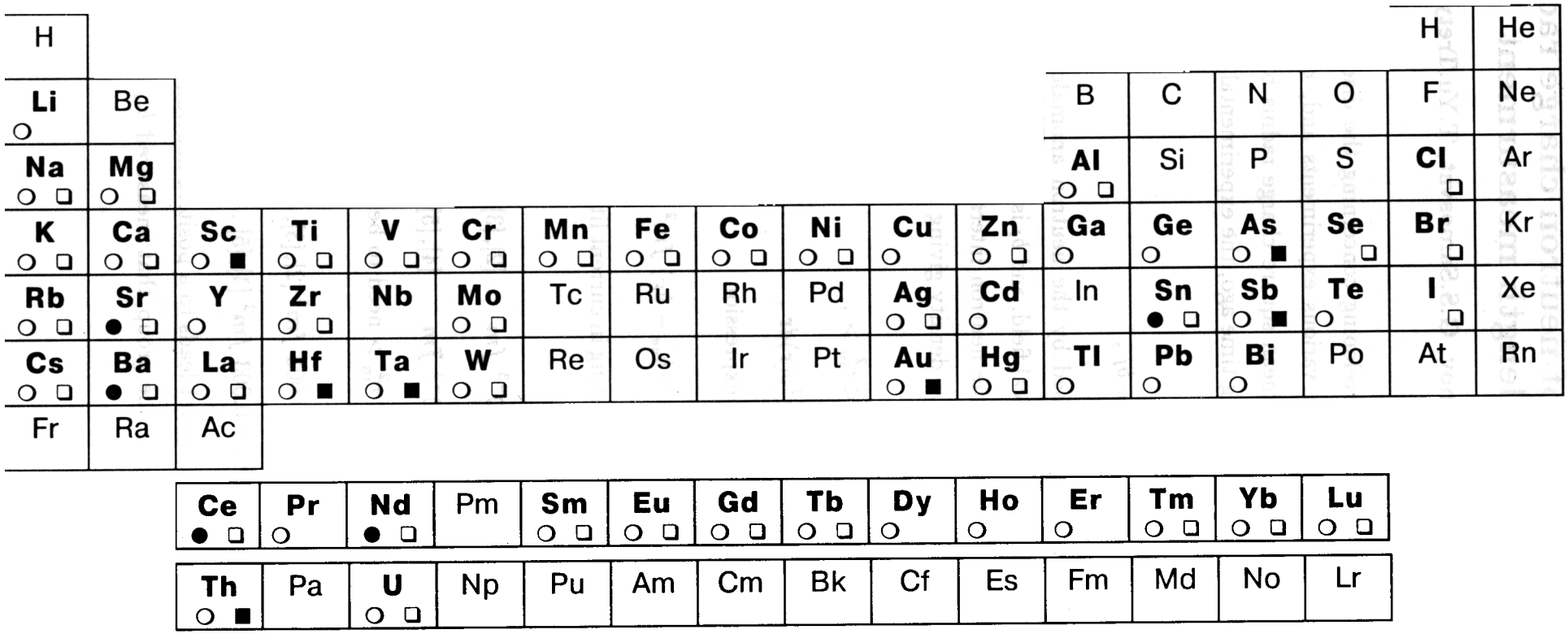

Fig. 1. Elements suitable for determination in moss by the present version of INAA (□) and by ICP-MS (❍). Closed symbols indicate the preferred method for the element in question.

On the estimate problem of neutron charge radius from (n,e)-scattering length measurment

G.G.Bunatian, V.G.Nokolenko, A.B.Popov, G.S.Samosvat, T.Yu.Tretyakova

Lately, an intense discussion has been developing concerning the discrepancies in the ne–scattering length data obtained from various experiments and, consequently, the controversial estimations of the neutron mean square charge radius based on b_{ne}–values. Having originated with Foldy [1] a long time ago, the experimental quantity b_{ne} is presumed to consist of two terms

$$b_{ne} \quad b_F + b_I \ ,$$

where b_F is the Foldy scattering length caused by the neutron anomalous magnetic moment μ interacting with the electron electrical field, and b_I is the scattering length — as though rendering an interaction between the neutron internal charge structure and an electrical field (strictly speaking, the charge density giving birth to this field). The following notations are used

$$b_I = \frac{1}{3}\frac{Me^2}{\hbar^2} < r_{in}^2 > \ ,$$

$$< r_{in}^2 >= \int r^2 \rho(\mathbf{r}) d\mathbf{r} \ ,$$

where M is the neutron mass. From this, the expression

$$< r_{in}^2 > \quad \frac{3\hbar^2}{Me^2} b_I \quad 86.4(b_{ne} \quad b_F) \ fm^2$$

appears. The experimental b_{ne} estimations existing in current literature are concentrated in the proximity of the two following values:

$$b_{ne} \quad (-1.59 \pm 0.04)10^{-3} \ fm \qquad [2], [3],$$

$$b_{ne} \quad -1.31 \pm 0.03)10^{-3} \ fm \qquad [4], [5]$$

Eventually, two estimations of the quantity $< r_{in}^2 >$ need to be discussed:

$$< r_{in}^2 > \quad 0.010 \pm 0.003 \ fm^2 \ [2], [3],$$

$$< r_{in}^2 > \quad +0.014 \pm 0.003 \ fm^2 \ [4], [5]$$

While no model of the nucleon structure yet leads to a positive neutron mean square charge radius, the Garching group [5] and the group that measured b_{ne} by means of

liquid ^{208}Pb at Oak Ridge [6] have given up accounting for the Foldy-term (the first using vague arguments [7] and the latter without any explanations at all), thereby reducing the definition of the neutron mean square charge radius to the expression

$$< r^2 > \quad \frac{3\hbar^2}{me^2} b_{ne} \ .$$

Under such circumstances, we are forced to face the primary sources of the problem and glance over the history to find the gist of the question.

Here, from the very first, it is necessary to determine the genuine relation between the measured ne–scattering length and the nucleon structure. In our opinion, there is a certain misunderstanding of this question [8] and we believe it will be instructive to trace back how this relation is acquired in various approaches. As the ne–scattering length is obtained from slow neutron scattering in the field produced by atomic electrons, the neutron interaction with an electromagnetic field will be described first.

A free nucleon, as well as any free particle with spin 1/2, is described by the Dirac equation. Yet the "external field" concept is limited and, generally speaking, untenable. In fact, even for an electron itself, the Dirac equation in the face of an external electromagnetic field $A = (\Phi, \mathbf{A})$

$$i\hbar\frac{\partial\psi}{\partial t} = (c\boldsymbol{\alpha}(\mathbf{p} - \frac{e}{c}\mathbf{A}) + \beta mc^2 + e\Phi)\psi,$$

$$i\hbar\frac{\partial\phi}{\partial t} = \mathcal{H}\phi,$$

$$\mathcal{H} \approx \frac{1}{2m}(\mathbf{p} - \frac{e}{c}\mathbf{A})^2 + e\Phi - \frac{\mathbf{p}^4}{8m^3c^2}$$

$$\frac{e\hbar}{2mc}\boldsymbol{\sigma}\mathbf{H} - \frac{e\hbar}{4m^2c^2}\boldsymbol{\sigma}[\mathbf{E}\times\mathbf{p}] - \frac{e\hbar^2}{8m^2c^2}div\mathbf{E} \qquad (1$$

(where $\mathbf{E} = -(\nabla\Phi)$, $\mathbf{H} = [\nabla \times \mathbf{A}]$, $\frac{e\hbar}{2mc} = \mu_0$, $\boldsymbol{\alpha}, \beta$ are Dirac matrixes, $\boldsymbol{\sigma}$ is the Pauli matrix, and ϕ is the large component of the bispinor ψ) does not enable to describe properly the properties of this point-like particle, because self-coupling to its own electromagnetic quantum field (radiative corrections) [9] is known to result in the additional terms in the equation to describe the behaviour of the electron in an external field A. The last three terms in $\mathcal{H}$ in eq. (1) are thus replaced by

$$-(\frac{e\hbar}{2mc} + \mu_e')\boldsymbol{\sigma}\mathbf{H} - \frac{1}{2mc}(\frac{e\hbar}{2mc} + 2\mu_e')\boldsymbol{\sigma}[\mathbf{E}\times\mathbf{p}] - \frac{\hbar}{\quad}(\frac{e\hbar}{\quad} + 2\mu_e')div\mathbf{E}, \qquad (1a)$$

where $\mu_e' = \frac{1}{2\pi}(\frac{e^2}{\hbar c})\frac{e\hbar}{2mc} + \ldots$ is the electron anomalous magnetic moment.

It is to emphasize here that in accounting for the radiative corrections, the coefficients prefixed to $\boldsymbol{\sigma}\mathbf{H}$ and to $div\mathbf{E}$ and $\boldsymbol{\sigma}[\mathbf{E}\times\mathbf{p}]$ are modified in different ways: the anomalous

magnetic moment μ'_e has been added to the magnetic moment $\frac{e\hbar}{2mc}$ in the term containing $\mathbf{H}$, whereas a twofold quantity has been added to the coefficients in two latter terms. Thus, it is quite impossible for even an electron to obtain eq. (1a) from eq. (1), that is, to account for the electron interaction with quantum fields (the radiative corrections) merely by replacing the magnetic moment of the point-like particle in the Dirac equation by the total magnetic moment that incorporates the anomalous one as well.

In a general form, the behaviour of a particle with spin 1/2 can be described in a formal way by means of the relativistic and gauge invariant equation [1], [9]

$$i\hbar\frac{\partial\psi}{\partial t} = \mathcal{H}\psi \quad [c\boldsymbol{\alpha}(\mathbf{p} - \frac{e}{c}\mathbf{A}) + \mu\beta(\boldsymbol{\Sigma}\mathbf{H} - i\boldsymbol{\alpha}\mathbf{E}) + \beta Mc^2 + e\Phi - \epsilon\Box\Phi + \epsilon\boldsymbol{\alpha}\Box\mathbf{A}]\psi, \quad (2)$$

where we restrict ourselves to accounting for the first order terms in field A and the D'Alamber operator $\Box$ only; here $\boldsymbol{\Sigma}$ is the spin operator and $F^{\mu\nu}$ is the electromagnetic field tensor. The lowest approximation in $1/c$ runs as follows

$$i\hbar\frac{\partial\phi}{\partial t} = \mathcal{H}\phi,$$

$$\mathcal{H} \approx \frac{1}{2M}(\mathbf{p} - \frac{e}{c}\mathbf{A} + \frac{\epsilon}{c}\Box\mathbf{A})^2 + e\Phi \quad (\frac{e\hbar}{2Mc} + \mu)\boldsymbol{\sigma}\mathbf{H} -$$

$$\frac{1}{2Mc}(\frac{e\hbar}{2Mc} + 2\mu)\boldsymbol{\sigma}[\mathbf{E}\times\mathbf{p}] - [\epsilon + \frac{\hbar}{4Mc}(\frac{e\hbar}{2Mc} + 2\mu)]div\mathbf{E}. \quad (2a)$$

In such a purely phenomenological approach, the empirically introduced parameters μ, ϵ render both the internal structure of a particle and its interaction with a vacuum of the electromagnetic and other quantum fields, which are not taken into account in the Dirac equation (1). The physical meaning of the quantity μ emerges unambiguously as the coefficient prefixed to $\boldsymbol{\sigma}\mathbf{H}$ in eq. (2a). Consequently, it is understood to be the "nucleon anomalous magnetic moment", completing the magnetic moment $\frac{e\hbar}{2Mc}$ of a point-like particle with spin 1/2, mass M and charge e. Yet, according (2a), this empirically introduced quantity μ shows up to determine not only the interaction of the particle with a magnetic field, but with an electrical field $\mathbf{E}$, as well: the "Schwinger interaction" (next to last term in eq. (2a)) and the "Foldy interaction" [1] (last term in (2a)). Certainly, expression (1a) for an electron ($\mu = \mu'_e$) corresponds completely with the general phenomenological equations (2), (2a).

As far as the parameter ϵ is concerned, no unambiguous conclusion about its physical contents can be drawn immediately from eqs. (2), (2a). The fact that ϵ is incorporated side by side with the terms containing μ in the coefficient prefixed to $div\mathbf{E}(\mathbf{R}) = -\triangle_R$

$\Phi(\mathbf{R}) = -4\pi\rho_e(\mathbf{R})$ in eq. (2a) ($\rho_e(\mathbf{R})$ is the charge density inducing the electric field) does not constrain the equation

$$\epsilon = \frac{1}{6}\int d\mathbf{r}\mathbf{r}^2\rho_n(\mathbf{r}),$$

(here ρ_n- is the density of the charge distribution inside the nucleon), contrary to what was presumed in [1], [8], and [10], as well as in some other publications. In such a phenomenological approach, this quantity ϵ is, as a matter of fact, a fitted-parameter that is allowed to take any value, including zero.

The interaction represented by the last term in eq. (2a) results in the Born amplitude of neutron scattering ($e = 0$)

$$f_{ne}(\mathbf{q}) \qquad \frac{2M}{\hbar^2}[\epsilon + \mu\frac{\hbar}{2Mc}]\int d\mathbf{R}e^{-i\mathbf{qR}}\rho_e(\mathbf{R}$$

in the field, induced by the charge density $\rho_e(\mathbf{R})$, and in particular by the charge distribution of the atomic electrons, the atom being nailed down (bound). With the quantity μ being equal to the experimental value of the neutron anomalous magnetic moment, and the quantity ϵ is assumed to be equal to zero, the ne–scattering length $b_{ne} = -f_{ne}(0)/Z$ proves to be equal to the value $b_{ne} = -1.468\,10^{-16}cm$, coinciding within a small error with up to date experimental results [2] - [7]. This is evidence that the ϵ value is small. However, pursuing this phenomenological approach, no rigorous conclusion about the nucleon structure can be acquired through this result. Certainly, as it was already emphasized long before [1], an approach can not been asserted as expedient if the coefficients assigned to describe the nucleon structure are introduced purely empirically and are never gained through any more-or-less general and profound physical theory or, at least, a model.

As pointed out above, accounting for radiative corrections for the electron itself modifies the coefficients by $\mathbf{H}$ and by $div\mathbf{E}$ in different ways. All the more, when the nucleon, being a much more complicated composite system, interacts with an external electromagnetic field, its structure can not be taken into account merely through modification of the Dirac equation, in particular, through replacement of the point-like-particle magnetic moment by the total one, including the anomalous one as well. At this time, because of the lack of a rigorous, thorough theory, the nucleon structure is investigated in the framework of various approaches and models.

The consideration of the magnitude of the ne-scattering amplitude in the framework of the Cloudy Bag Model **CBM** [11],[12] does nothing proportional to the μ $div\mathbf{E}$ (like (4)) contribution to the ne–scattering amplitude. By the way, it might be instructive

here to point out that the question about the "Foldy term" in the electron–nucleon interaction has never arisen, while the Lamb shift is investigated in either the ordinary or in the mesonic atoms (see, for example, [13]). On the other hand, in the framework of the phenomenological Foldy approach [1], the ne–scattering amplitude is expressed through the quantity μ according to eq. (4), yet nothing can be concluded immediately about the hidden physical sense of the quantity ϵ, namely that this approach is only phenomenological. Foldy himself, suggesting eq. (3) as being the plausible physical representation for the quantity ϵ, had, as a matter of fact, only designated such an interpretation, but never made any concise statements. Instead he referred to experiments to disentangle the physical meaning of the quantity ϵ. For years, in successive works, the quantity ϵ has been assumed to be exactly equal to the value of the second momentum of the nucleon charge distribution (3), no new or additional argument having been managed at all.

Obtaining $< r_n^2 >$ with high precision experimentally will promote, in our opinion, the development and improvement of the various models now suggested for describing the nucleon, ignoring for the moment that these approaches are apparently not yet in position to provide an accuracy better than $\sim$ 10%. Beyond question, any theoretical approach must be able to successfully describe not only one characteristic of the nucleon, but the majority of the following, simultaneously: $< r^2 >$, μ , m_N , g_A, and so on. Therefore, it is desirable to obtain the values of all of these quantities from experimental data with equal precision. Specifically, the $< r^2 >$ value needs to be known to the same accuracy as the values of μ, g_A and so forth.

On the other hand, exact determination of the ϵ value will enable us to judge to what degree the anomalous magnetic moment incorporates all the main features and peculiarities of the neutron structure while describing, according to aforecited phenomenological approach, the behavior of a neutron in an external electromagnetic field. If the ϵ value proves to be very small, almost negligible, an amazing and intriguing conclusion will be inescapable: that the spectacular phenomenological approach really does exist in which the anomalous magnetic moment thoroughly renders the structure of the neutron as it interacts with an external electromagnetic field. The goals of further experimental investigations are to obtain the b_{ne} value with better accuracy than before and that these measurements will not require significant corrections in the processing their results.

The research described in this publication was made possible in part by Grant RFS000 from the International Science Foundation and by Grants 94-02-03118 and 96-02-16538 RFFI.

References

[1] Foldy L., Phys.Rev. **87**, 688 (1952); Phys.Rev. **87**, 693 (1952); Rev.Mod.Phys. **30**, 471 (1958)

[2] Melkonian E., Rustad B.M., Havens W.W., Phys.Rev. **114**, 1571 (1959)

[3] Alexandrov Yu. A., Machekhina T. A., Sedlakova L. N., Fykin L. N., Yadernaya Fisika, **20**, 1190 (1974); Sov. J. Nucl. Phys. **60**, 623 (1975)

[4] Krohn V.E., Ringo G.R., Phys.Rev. **D8**, 1305 (1973)

[5] Koester L., Waschkowski W., Kluver A., Physica, **137B**, 282 (1986)

[6] Kopecky S., Riehs P., Harvey J., Hill N., Phys.Rev.Lett. **74**, 2424 (1995)

[7] Koester L., Waschkowski W., Mitsyna L.V., Samosvat G.S., Prokofjevs P., Tambergs J., Phys.Rev. **C51**, 3363 (1995)

[8] De Benedetti S., "Nuclear Interections", John Wiley & Sons, New York, 1968;
Frauenfelder U., Henley E., "Subatomic Physics", Ch.VI, Prentice-Hall, Inc., New Jersey, 1974;
Alexandrov Yu. A., "Fundamental Properties of the Neutron", Energoizdat, Moscow, 1982; Clarendon Press, Oxford, 1992;
Gurevich I.I., Tarasov L.V., "Neutron Physics", Nauka, Moscow, 1965;
Alexandrov Yu.A., Neutron News, **5**, iss. 1, 20 (1994), **5**, iss.4, 17 (1994);
Byrne J., Neutron News, **5**, iss. 4, 15 (1994)

[9] Achieser A.I., Berestezky V.B., "Quantum Electrodynamics", "Nauka", Moscow, 1969.
Berestezky V. B., Lifshiz E. M., Pitaevsky L. P., "Relativistic Quantum Theory", "Nauka", Moscow, 1968.

[10] Sears V.F., Phys.Reports, **141**, 281 (1986)

[11] Thomas A. W., Adv. Nucl. Phys. **13**, 1 (1984)

[12] Bunatian G.G., Sov. J. Nucl. Phys., **46**, 188 (1987); **48**, 820 (1988); **51**, 637 (1990); Nucl. Phys., **A509**, 736, (1990)

[13] Borie E., Phys. Rev. Lett., **47**, 568 (1981)

ENERGY DEPENDENCE OF FISSION FRAGMENT ANGULAR ANISOTROPY IN RESONANCE NEUTRON INDUCED FISSION OF ^{235}U

W.I.Furman[1)], N.N.Gonin[2)], J.Kliman[3)], Yu.N.Kopach[1)], L.K.Kozlovsky[2)], A.B.Popov[1)], H.Postma[4)], D.I.Tambovtsev[2)].

1) FLNP JINR ,Dubna, Russia
2) RRC IPPE, Obninsk, Russia
3) IP SAS, Bratislava, Slovakia
4) TU Delft, Netherlands

The investigation [1] of energy dependence of fission fragment angular anisotropy in slow neutron induced fission of the ^{235}U aligned target was continued at the pulsed neutron source IBR-30 of the FLNP. The measurements were performed using a new dilution refrigerator with improved target consisting of two mosaics of monocrystals of uranyl rubidium nitrate mounted onto a copper backing, cooled down to a temperature of ~0.1 K to ensure an alignment of uranium nuclei. The processing of both new and earlier obtained [1,2] data was realized by a new algorithm, when the relative angular anisotropy A_2 was obtained as function of the neutron energy for each experimental run separately and thereafter averaged over all runs. The absolute scale of the A_2 values was chosen from a comparison of our average value with the one from [3]. The statistical accuracy was about 3-10 % for the energy bins of 0.05 eV in the region 0.04-10 eV.

The results [3] interpreted by the authors under the assumption that the angular anisotropy coefficient A_2 could be defined for a given resonance λ by the formula

$$A_{2\lambda}^{JK} = \sum_K A_2^{JK}\,\Gamma_{f\lambda}^{JK}/\Gamma_{f\lambda}^{J} \qquad 1)$$

where the factor A_2^{JK} is determined by the Racah and Clebsch-Gordan coefficients, which depend only on spin J and its projection K on the fission axis of the compound state under consideration. The contribution of the specific state λ is defined only by the ratio of the partial $\Gamma_{f\lambda}^{JK}$ to total $\Gamma_{f\lambda}^{J}$ fission widths. As a result of the analyses [3,4] it was concluded in [4] that in the s-wave resonance neutron induced fission of ^{235}U only fission channels with K=1 and K=2 are open for both compound state spins J=3 and 4. At the same time for states with J=3 an admixture of the channel K=0 is possible.

The new approach to the theoretical description of fission process using the microscopic representation of fission fragment channels and their convolution to the observed JK-channels led to the modified formulae for differential fission cross-sections induced by slow neutrons [5] :

$$\frac{\partial\sigma_{nf}(E)}{\partial\Omega} = \frac{1}{4\pi}\left[\sigma_{f0}(E) + f_2\sigma_{f2}(E)P_2(\cos\theta)\right], \qquad (2)$$

where

$$\sigma_{f0} = \frac{\pi}{k^2}\sum_J g_J \sum_K \left|S^J(0\tfrac{1}{2} \to Kf)\right|^2 \qquad (3)$$

is the total fission cross-section and

$$\sigma_{f2} = G\frac{\pi}{k^2}\sum_{JJ'}\sqrt{g_J g_{J'}}U(\frac{1}{2}IJ'2;JI)\sum_{K}C^{J'K}_{JK20}S^{*J'}(0\frac{1}{2}\rightarrow Kf)S^{J}(0\frac{1}{2}\rightarrow Kf) \quad (4)$$

takes place due to an alignment of the target nucleus spin I. Here symbols f_2 and $P_2(\cos\theta)$ denote the alignment coefficient [3] and the Legendre polynomial respectively. In (2) - (4) the g_J and G are the statistical and geometric normalization factors defined by

$$g_J = (2J+1)/2(2I+1) \quad \text{and} \quad G = \frac{15I^2}{\sqrt{(2I+1)I(I+1)(2I+3)}},$$

and $k = (2mE/h^2)^{1/2}$ is the wave number of incident neutrons. Symbols $U(1/2IJ'2;JI)$ and C^{JK}_{JK20} are the Racah and Clebsch-Gordan coefficients . The dynamics of the reaction is included via the S-matrix elements $S^J(lj \rightarrow Kf)$ which define the probability of a transition from the entrance neutron channel characterized by the orbital l and total j angular momenta of the neutron to the fission channel JK (for more detail, see [5]) .

With the aid of formulae (2)-(4) it is possible to define the angular anisotropy of fission fragments in a consistent way as

$$A_\gamma(E) = \frac{\sigma_{f2}(E)}{\sigma_{f0}(E)}$$

This formula allows one to assume that due to the interference of different resonances the $A_2(E)$ value is determined not only by the partial and total fission widths of the nearest resonance, as in formula (1), but depends essentially on the partial amplitudes $\sqrt{\Gamma^{J\pi K}_{\lambda f}}$ of all neighboring resonances. Besides, one should expect an influence of the effects from the interference of s-wave neutron resonances with different spins on the behavior of the $A_2(E)$.

For the analysis of the experimental data on the A_2 (E) values a special code was developed with the S-matrix parametrization proposed for the ENDF/B-VI library:

$$S^J_{cc'} = e^{-(\phi_c-\phi_{c'})}\left\{2\left((I-\tilde{K})^{-1}\right)_{cc'} - \delta_{cc'}\right\} \quad (6)$$

For neutron induced fission we have:

$$S^J_{nf} = 2e^{-i\phi_n}W^J_{nf} \quad (7)$$

(ϕ_f=0 for the fission channel, as shown in [5] and

$$W^J_{nf} = \left((I-\tilde{K})^{-1}\right)_{nf}$$

where

$$(I-\tilde{K})_{cc'}=\delta_{cc'}-\frac{i}{2}\sum_{\lambda}\frac{\sqrt{\Gamma^{J}_{\lambda c}}\sqrt{\Gamma^{J}_{\lambda c'}}}{E_{\lambda}-E-i\Gamma_{\lambda\gamma}/2} \qquad (9)$$

The function $A_2(E)$ was calculated by formulae (2) - (9). The fission channels with JK = 30, 31, 32, 41 and 42 were included in the calculations. Doppler broadening and the resolution function of the spectrometer were taken into account, as well. With the aid of the described procedure our data on the $A_2(E)$ in the neutron energy range from 0.1 up to 10 eV were analyzed together with the data [6] for 0.04 - 1.5 eV . In the calculation, 22 resonances were taken into account : 16 resonances in the energy interval under investigation plus 2 "negative" resonances and 1 resonance above 10 eV for each spin, respectively.

We have made an attempt to fit simultaneously as the $\sigma_{f0}(E)$ and the $A_2(E)$ values in energy interval 0.1-10 eV as well as the spin-separated fission cross sections $\sigma^{3^-}_{f0}(E)$ and $\sigma^{4^-}_{f0}(E)$ for neutron energy 0.1-1.9 eV with the fixed positions , neutron and total radiative and fission widths of the resonances under investigation taken from [7]. The ENDF/B-VI data file for $\sigma_{f0}(E)$ and data from [8,9] for spin-separated cross sections $\sigma^{J\pi}_{f0}(E)$ were used. We varied firstly only signs and relative weights of a partial fission amplitudes for all resonances mentioned above. It turned out to be impossible to fit the $A_2(E)$ dependence in the framework of this procedure. Thus all parameters of negative resonances and total neutron and fission widths of some positive resonances were „released" and new fit has be done taking care of the consistent description of the integral and spin-separated fission cross sections.

Fig. 1 shows the results of the $A_2(E)$ fitting where the points and curves represent, respectively, the experimental data and two variants of the fit. The calculations show significant sensitivity of the $A_2(E)$ to small variations of as neutron and as well as fission amplitudes and their signs. One of the main conclusions which has to be made is that the effects of interference between resonances have really strong influence on the structure of the $A_2(E)$. The effect of interference of resonances with different spins is also essential. The calculations demonstrate 10-20% variations in the $A_2(E)$ behavior after including of the JJ' terms in the σ_{f2} (compare the solid and dotted lines in Fig. 1). It is worth to note that hi-square values per point (including the σ_{f0} and $\sigma^{J\pi}_{f0}$ data) are 0.96 and 2.08 with and without accounting for the JJ' terms, respectively.

The "K-anatomy" of the A_2 fitted values is represented in Fig. 2 where contributions of different K projections (summed over J) to the total $A_2(E)$ dependence are apparently shown. It is clear that very peculiar energy dependence of the $A_2(E)$ function is the result of a rather irregular behaviour of its K-components. So it is obvious that the previous idea [3], that one can attribute a $A_{2\lambda}$ value (1) to each resonance λ connected only with its fission widths, is hardly correct since for any given energy the $A_2(E)$ is „formed" by a group of neighboring levels.

After this analysis very important problems still remain. They are the question of uniqueness of the fitted parameter set and the consistence of these calculations with the description of the neutron capture and transmission data. It is necessary also to include in the fitted data the spin-separated fission cross sections for neutron energy up to 10 eV. In any case, the analysis outlined above permits, in principle, to extract unambiguously the partial fission amplitudes of s-wave neutron resonances and gives

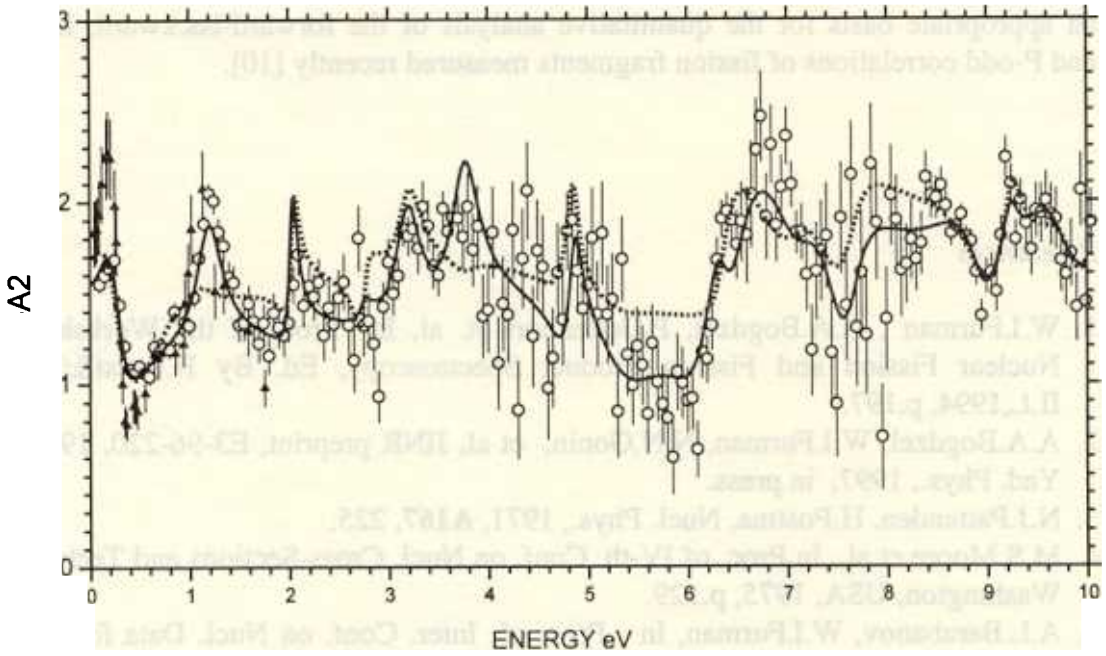

The dependence of the angular correlation between spin orientation of target 235U nucleus and fission fragment momentum on neutron energy. Experimental data: circles - present work, the fit: solid line - with JJ'-interference, dottted one - without it.

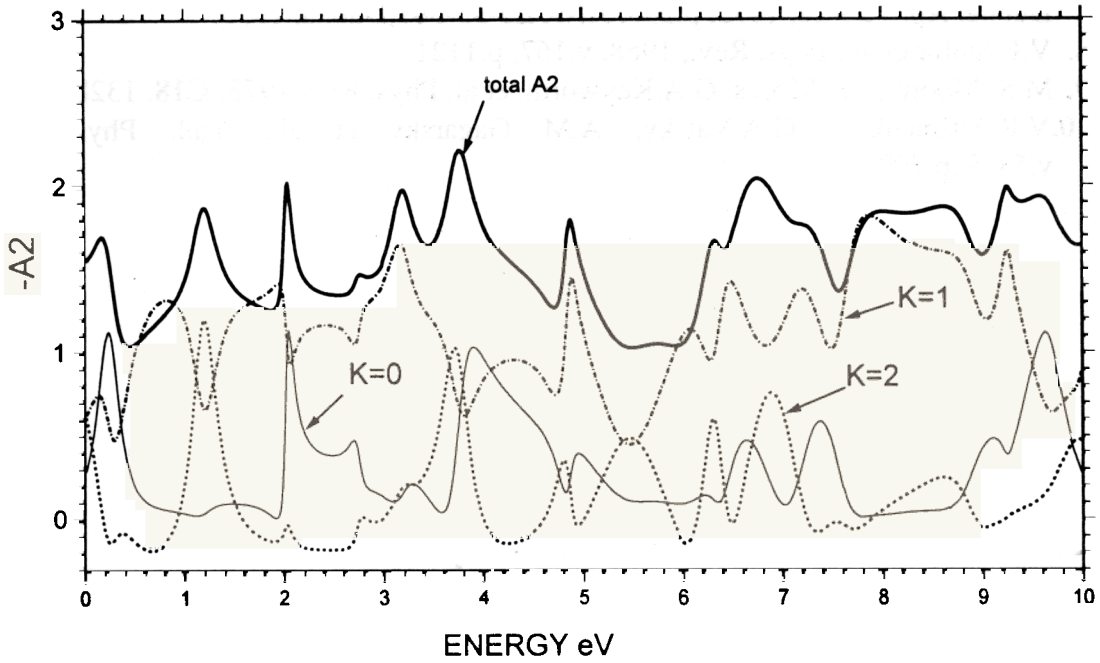

The contributions of diffrent K-projections in the A2(E).

an appropriate basis for the quantitative analysis of the forward-backward, left-right and P-odd correlations of fission fragments measured recently [10].

References

1. W.I.Furman , A.A.Bogdzel, P.Geltenbort et. al, In Proc. of the Workshop on Nuclear Fission and Fission Product Spectroscopy, Ed. By H.Faust&G.Fioni, ILL,1994, p.197.
2. A.A.Bogdzel, W.I.Furman, N.N.Gonin, et al, JINR preprint, E3-96-220, 1996, and Yad. Phys., 1997, in press.
3. N.J.Pattenden, H.Postma, Nucl. Phys., 1971, **A167**, 225.
4. M.S.Moore et al., In Proc. of IV-th. Conf. on Nucl. Cross-Sections and Technology, Washington, USA, 1975, p.129.
5. A.L.Barabanov, W.I.Furman, In Proc. of Inter. Conf. on Nucl. Data for Science and Technology, Gatlinburg, Tennessee, Ed. by J.K. Dickens, 1994, v.1, p.448.
6. H.Postma, In Proc. Int. Symp. on Neutron Capture, Gamma Ray Spectroscopy and Related Topics, Petten, 1974, p.619.
7. M.S. Moore, In Proc. of III-th Inter. Seminar on Interaction of Neutrons with Nuclei, Dubna, April 26-28, 1995, p.290, JINR E3-95-307,Dubna, 1995.
8. V.L.Sailor et al., Phys. Rev., 1968, v.167, p.1121.
9. M.S. Moore , J.D.Moses, G.A.Keyworth et al, Phys. Rev. 1978, **C18**, 1328.
10. V.P.Alfimenkov, G.A.Valsky, A.M Gagarsky et al., Yad. Phys., 1995, v.58(5),p.799.